AD 290 058

UNCLASSIFIED

63-1-5

290 058

HUGHES TOOL COMPANY · AIRCRAFT DIVISION

Culver City, California

Contract No. AF 33(600)-30271

Report 285-9-7 (61-79)

HOT CYCLE ROTOR SYSTEM

RESULTS OF STATIC TEST PROGRAM GAS FLOWS AND TEMPERATURES

February 1962
Revised June 1962

HUGHES TOOL COMPANY -- AIRCRAFT DIVISION
Culver City, California

HUGHES TOOL COMPANY

AIRCRAFT DIVISION

For

Commander

Aeronautical Systems Division

Prepared by:

D. L. Jones
Head, Propulsion Group

J. W. Rabek
Aerodynamics Specialist

Approved by: Rodney A. Boudreaux
R. A. Boudreaux
Chief, Aerodynamics Section

J L Velazquez
J. L. Velazquez
Sr. Project Engineer

H. O. Nay
H. O. Nay
Manager, Transport Helicopter

FOREWORD

This report has been prepared by Hughes Tool Company - Aircraft Division under USAF Contract AF 33(600)-30271 "Hot Cycle Pressure Jet Rotor System", D/A Project Number 9-38-01-000, Subtask 616.

The Hot Cycle Pressure Jet Rotor System is based on a principle wherein the exhaust gases from high pressure ratio turbojet engine(s) located in the fuselage are ducted through the rotor hub and blades and are exhausted through a nozzle at the blade tip. Forces thus produced drive the rotor.

Summarized herein are the analyses and tests relating to determination of duct losses, nozzle coefficients and similar data used in analyzing the efficiencies of the Hot Cycle System. This report is in partial fulfillment of Item 6C, covering Component and Assembly Tests performed under Item 6a (4) and 7a of the contract.

ABSTRACT

This report provides an aerothermal survey (test and analysis) of the Hot Cycle whirl test system under static conditions and includes a tether test, hub cooling test, and J57 gas generator calibration. Emphasis is placed on correlation of test data with earlier derived values used in performance predictions. In general, agreement between predicted and measured values of duct losses, nozzle coefficients and tip thrust was realized. Most significant, the tip nozzle effective velocity coefficient, directly proportional to tip thrust, was measured to be 0.98, 2.5% better than predicted. Hub cooling is shown to be satisfactory and no overtemperaturing of hub or spar components has been encountered. The normal engine operating line, including turbine discharge pressure and temperature versus high pressure compressor rpm, has been established. Also, exhaust valve controlled "off-line" turbine discharge temperatures have proven to be sufficient to meet contractual requirements.

TABLE OF CONTENTS

LIST OF FIGURES

LIST OF FIGURES (Continued)

LIST OF TABLES

I. INTRODUCTION

The Hot Cycle Helicopter whirl test installation is shown in Figure 1 and internal views of the control van are presented in Figure 2. To determine the thrust, pressure loss, and temperature characteristics of the primary and secondary flow circuits of the rotor system, as well as the effect of exhaust dump valve position on the Pratt and Whitney J57 engine's performance, a number of tests were performed as follows:

a. Tether Test - The rotor was attached to a fixed jig by a cable on which a tension load cell was attached. Flow was allowed in one blade only by sealing the remaining two. Calibrated strains in the load cell then permitted a direct measurement of the thrust of one blade. This electro-mechanical measurement coupled with flow, pressure, and temperature measurements provided the required data to determine tip nozzle coefficients. The flow measurements allowed a check on the suitability of the provided flow instrumentation and the pressure and temperature measurements gave a check on pressure and temperature losses in some duct components.

b. Hub Cooling Circuit Calibration - With the blades non-rotating, ducts were attached to the exhaust ports of the hub cooling circuit to simulate the centrifugally pumped cooling air by artificial suction. Through this simulation, the hub cooling circuit was calibrated to determine whether the cooling passages were appropriately sized.

c. J57 Engine Performance - With the vertical duct valve closed, the J57 was operated at military power with the exhaust dump valve in a number of positions to determine the effect of this latter valve on the J57's exhaust temperature and pressure. This was done in order to ascertain whether the

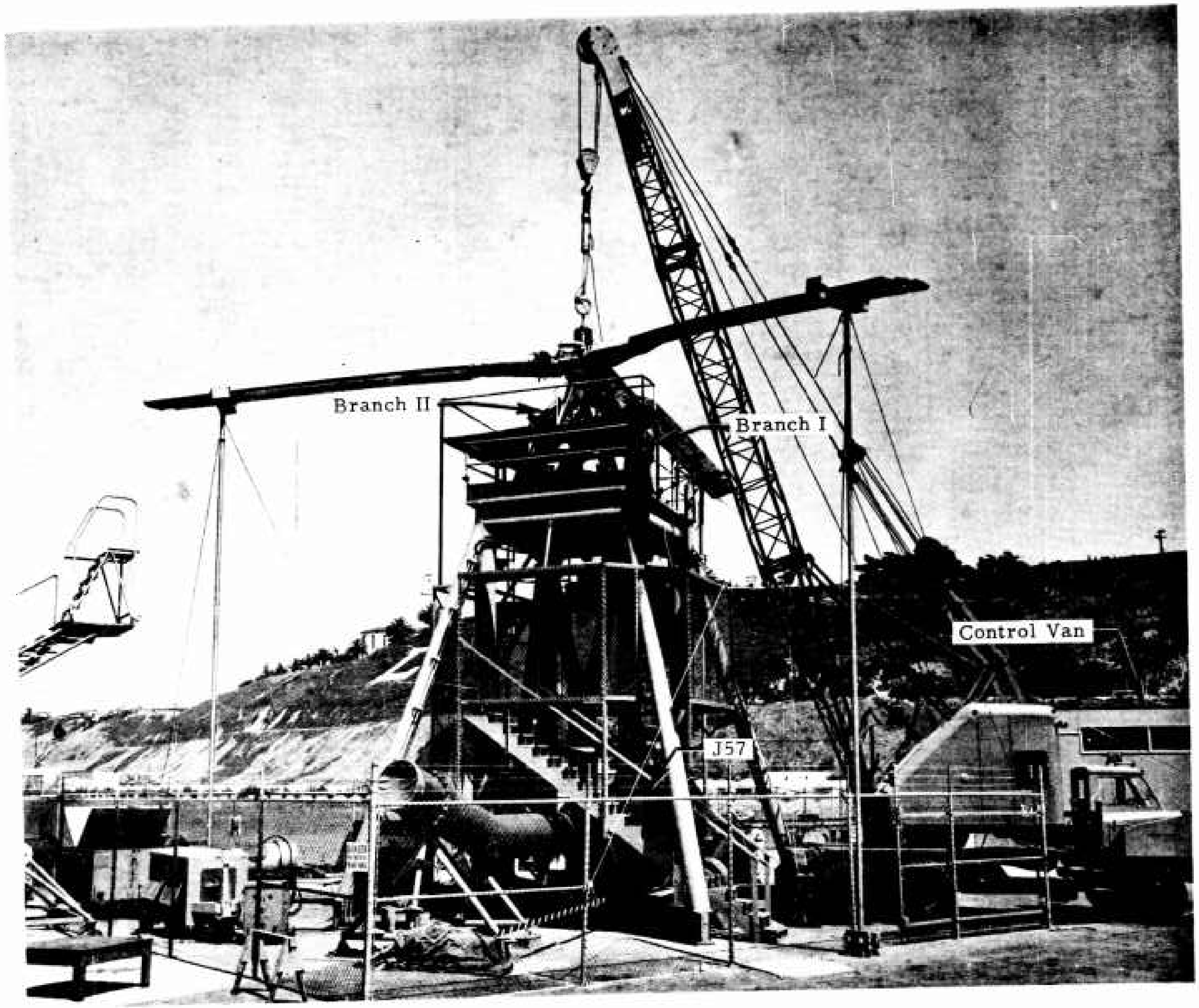

Figure 1. Hot Cycle Helicopter Whirl Test Installation

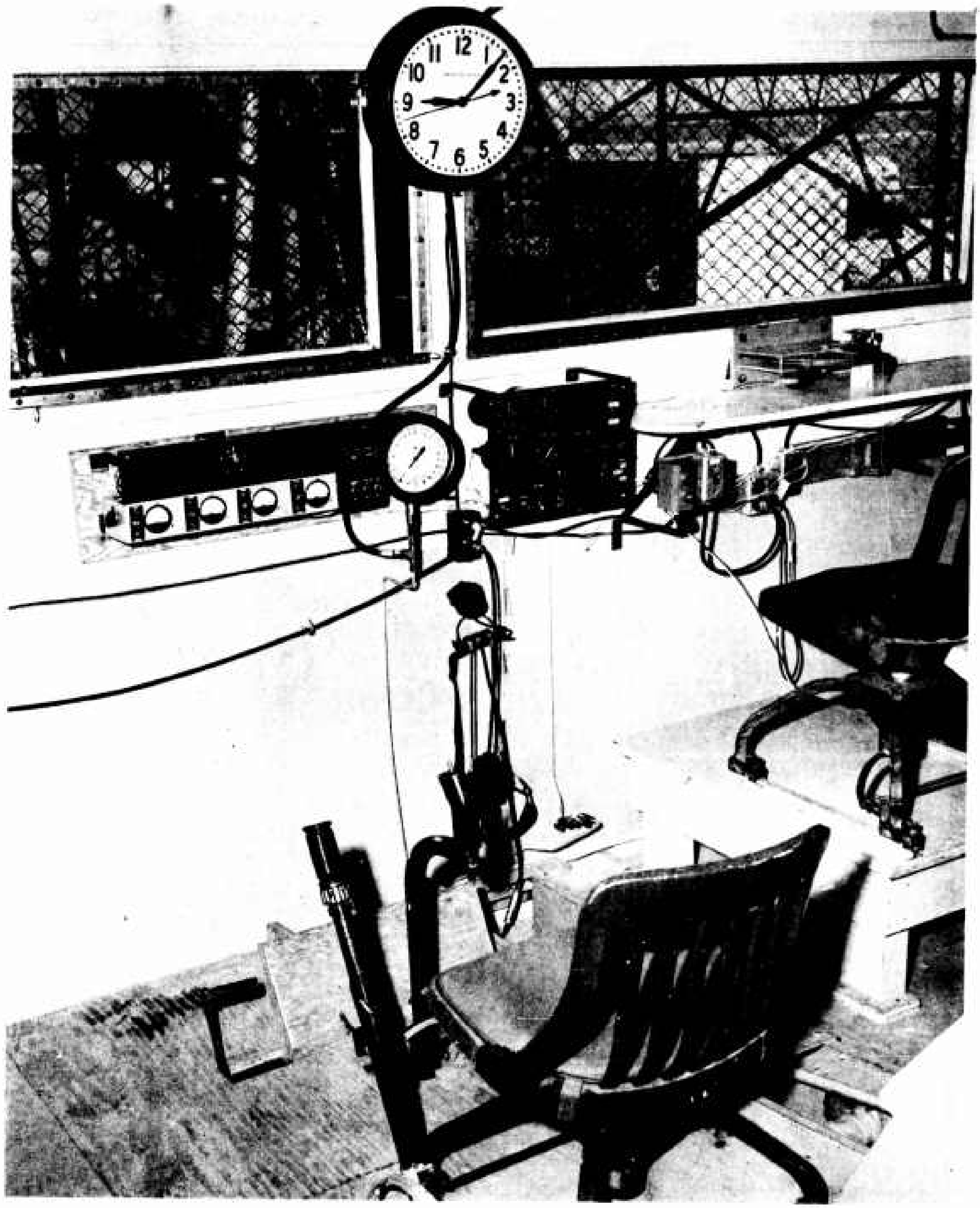

Figure 2, a. Internal View of Control Van-Engine and Rotor Controls

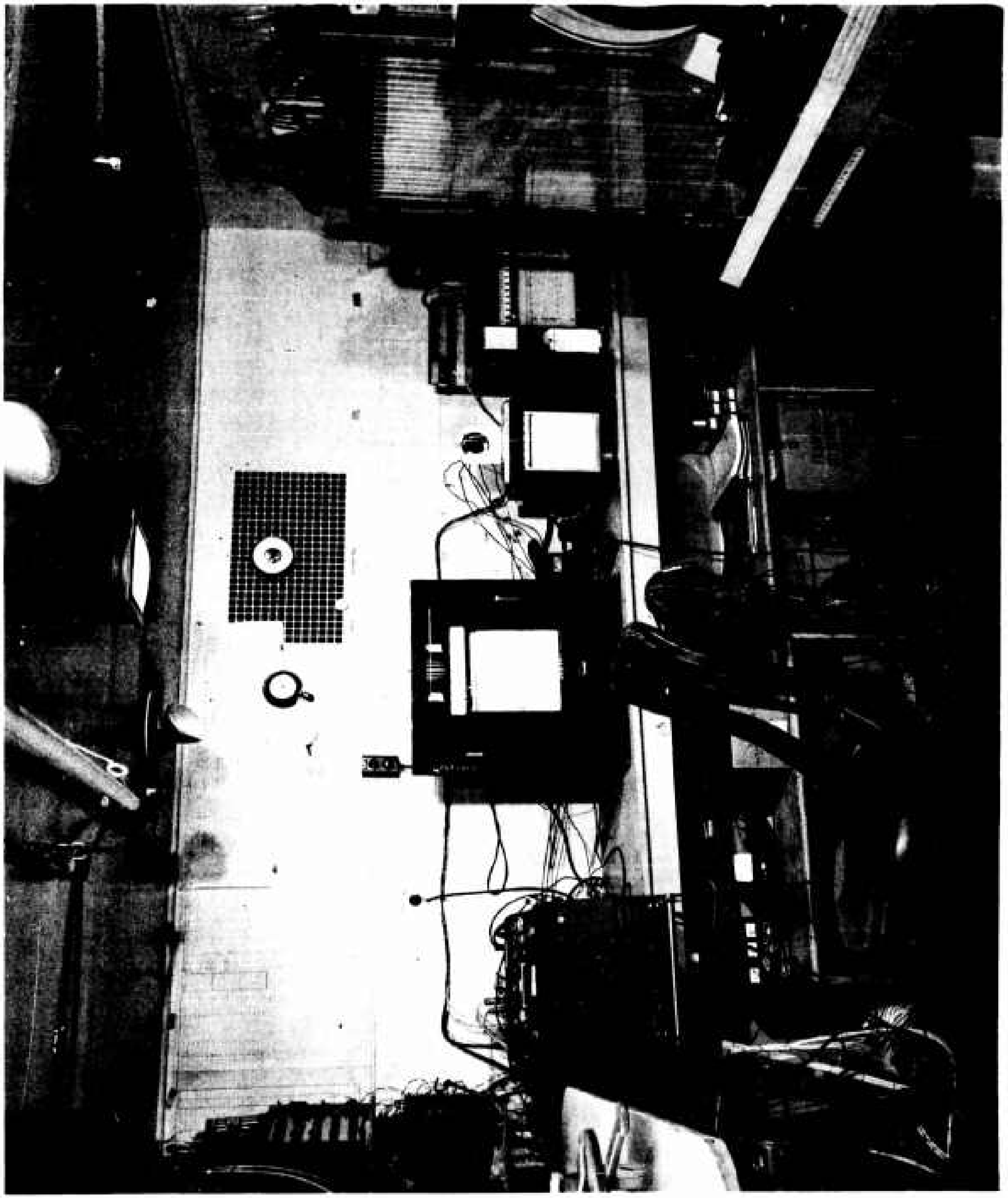

Figure 2, b. Internal View of Control Van-Temperature, Pressure and Strain Recording Instruments

J57 could suitably approximate the exhaust conditions of the Hot Cycle design (based on the General Electric T64 engine) by operation nearer to the J57 stall line.

This report provides test results and accompanying analyses to determine the "as built" aerothermal parameters of the hot cycle system. Discussed also, is the connection of these parameters to test conditions studied and to setup limitations.

2. PRIMARY DUCT PRESSURE LOSS CHARACTERISTICS

The tether test data of Sections 3 and 4 provide pressure losses of the primary flow system. Total pressure was measured at the following stations:

a. Ambient (P_o)

b. Turbine discharge (P_{t_7})

c. Flow measuring stations in Branches I and II $(P_{t_{fs}})_{I \text{ and } II}$

d. Hub; below rotating seal in each branch $(P_{t_{hub}})_{I \text{ and } II}$

e. Nozzle inlet in each duct of one blade $(P_{t_{nozz}})_{LE \text{ and } TE}$

From Table 3, comparison of Columns 16 and 17 or 19 and 20 shows that the flow rates in the two stack branches are approximately 3:1 (Branch II:Branch I). This is due to the relative position of the tested blade to the whirl stand. The two stack ducts join at the hub to provide a flow cross section which is an annulus split into two 180° segments (Figure 3). The three blades join at the hub and form an annular flow cross section which is divided into three 120° segments. These two sets of segments are coupled at the rotating seal and had a relative position of blades to the stand (stack ducts) as in Figure 3 thereby favoring flow from Branch II.

Table I provides the loss characteristics of the ducts for the first nine runs of the tether test runs for which all instruments were installed and operating. Although the value of R, γ, streamwise temperature ratios and mixing losses are not constant for each of these runs due to variable water injection, the pressure loss ratios ($\frac{\Delta PT}{P_{T_7}}$) are quite uniform. The pressure loss from the turbine discharge plane (P_{t_7}) to the hub stations is of the order of 6 to 7%. This is in good agreement with previous estimates although the flow for the tether test was to one blade instead of three. Agreement was found in spite of the apparent discrepancy in flow rates between design

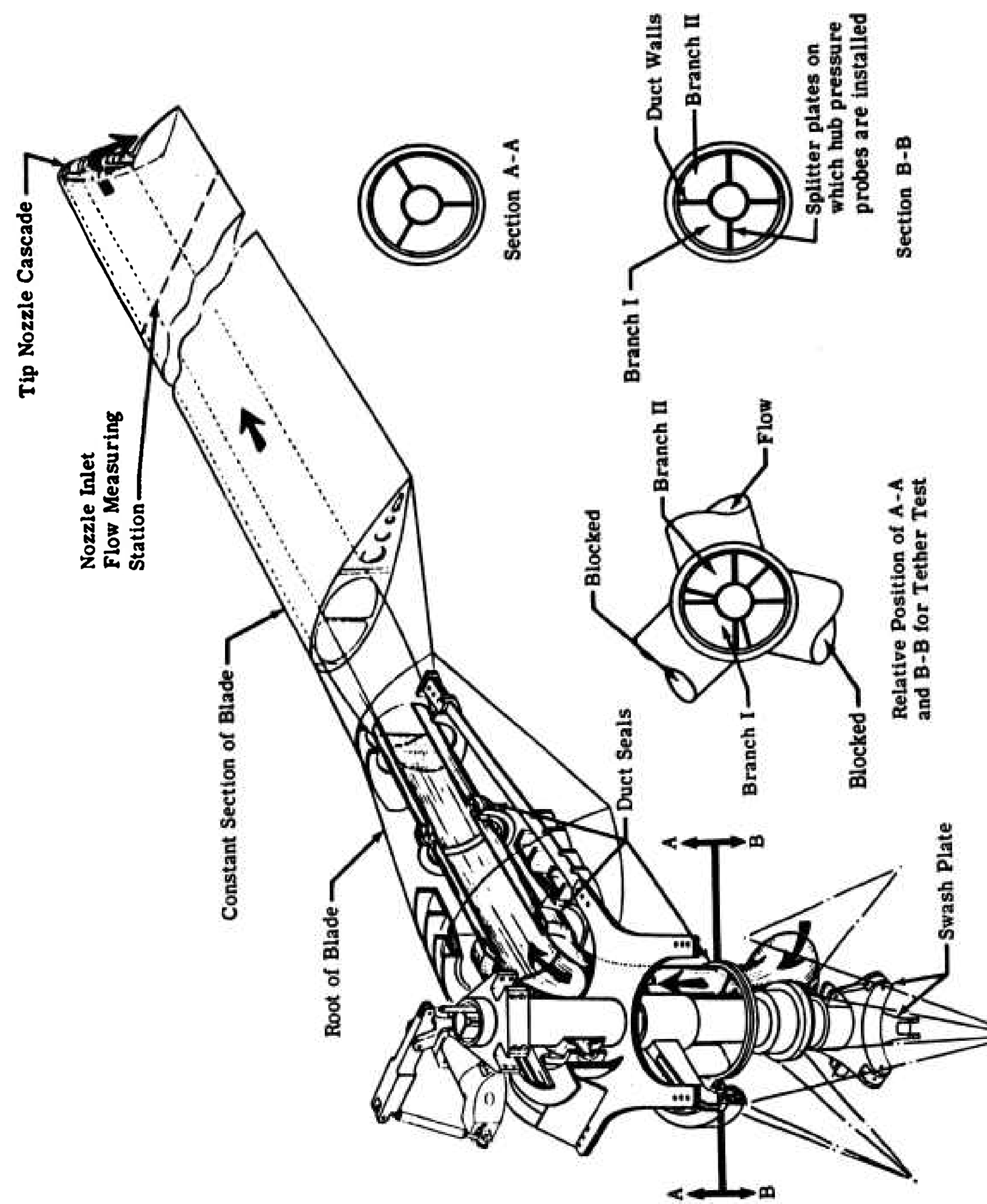

Figure 3. Primary Flow Path Through Hub

TABLE 1

Tether Test Streamwise Pressure and Pressure Loss Characteristics

	1	2	3	4	5	6	7	8	9	10	11	12	13	14
	P_o	P_{t_7}*	$P_{t_{fs_I}}$	$P_{t_{fs_{II}}}$	$P_{t_{hub_I}}$	$P_{t_{hub_{II}}}$	$P_{t_{nozz_{LE}}}$	$P_{t_{nozz_{TE}}}$	$\frac{P_{t_7}-P_{t_{fs_I}}}{P_{t_7}}$	$\frac{P_{t_7}-P_{t_{fs_{II}}}}{P_{t_7}}$	$\frac{P_{t_7}-P_{t_{hub_I}}}{P_{t_7}}$	$\frac{P_{t_7}-P_{t_{hub_{II}}}}{P_{t_7}}$	$\frac{P_{t_7}-P_{t_{nozz_{LE}}}}{P_{t_7}}$	$\frac{P_{t_7}-P_{t_{nozz_{TE}}}}{P_{t_7}}$
	psfa	psfa	psfa	psfa	psfa	psfa	psfa	psfa						
1	2117	3197	3020	3012	3020	2972	2676	2736	0.0554	0.0579	0.0554	0.0704	0.1630	0.1442
2	2118	3457	3291	3280	3291	3230	2861	2940	0.0480	0.0512	0.0480	0.0657	0.1724	0.1496
3.	2118	3774	3573	3560	3573	3505	3076	3144	0.0533	0.0567	0.0533	0.0713	0.1849	0.1669
4	2118	3990	3806	3792	3806	3729	3218	3224	0.0461	0.0496	0.0461	0.0654	0.1935	0.1920
5	2118	4206	3986	3971	3986	3908	3372	3481	0.0523	0.0559	0.0523	0.0709	0.1983	0.1724
6	2118	4552	4311	4295	4309	4227	3646	3740	0.0529	0.0565	0.0534	0.0714	0.1990	0.1764
7	2118	4854	4587	4572	4587	4499	3874	3971	0.0550	0.0581	0.0550	0.0732	0.2019	0.1819
8	2118	4955	4735	4715	4735	4623	3980	4093	0.0444	0.0483	0.0444	0.0670	0.1968	0.1740
9	2118	4984	4729	4712	4727	4630	3989	4103	0.0512	0.0546	0.0516	0.0710	0.1996	0.1768

* All total pressure values in this table are averages.

and test because the flow through one branch was three times as great as the other as explained earlier. Future whirl test data will provide more realistic flow rates and a closer check on predictions.

A comparison of Columns 9 and 11 (Table 1) indicates virtually no pressure loss between the flow measuring and hub stations of Branch I. This is caused by the low flow rates in that branch yielding pressure differentials below the accuracy of the instrumentation. The losses betweeen the hub station and the nozzle inlet plane are of the order of 14% P_{t_7} (average of Columns 13 and 14 minus average of 11 and 12), somewhat higher than the 10 to 12% expected for flow to three static blades. This is due to diverting the flow to one blade (area and direction change from design), and to the relative position of the tested blade and whirl stand as described earlier.

3. ROTOR TIP THRUST

Rotor tip thrust was measured as a function of turbine discharge pressure and corresponding engine operating line temperatures up to 770°F without water injection for cooling. For higher pressures resulting in higher turbine discharge temperatures, water injection was employed to maintain blade temperatures below 800°F.

Blocking the flow to two of the three blades enabled a study of the tip thrust characteristics of a single blade. Although compromises, such as one feeder stack being under-fed, and high hub pressure losses resulted, the utilization of a single blade simplified the artificial skin cooling requirements (water spray) and effectively reduced the data analysis to one-third.

The tested blade was tethered as in Figure 4, the tension load cell being 90° to the blade at Station 320R. Nozzle instrumentation as discussed in Section 4 was installed for Runs 1 through 22 of Table 2 and were removed for Runs 23 through 27 to determine whether the instrument leads, having been directed through the cascade, had affected the thrust. Pertinent thrust and flow data is included in that table.

A comparison of the instrument blockage effect on rotor thrust as a function of turbine discharge pressure is presented in Figure 5. In the choked range, the uninstrumented runs provide approximately 4% more thrust.

The maximum thrust recorded was 702 lb. per blade. This value, in presence of the amplified duct losses, is lower than the maximum predicted for normal flow conditions, but compares quite favorably with the thrust computed assuming similar temperature and pressure ratio.

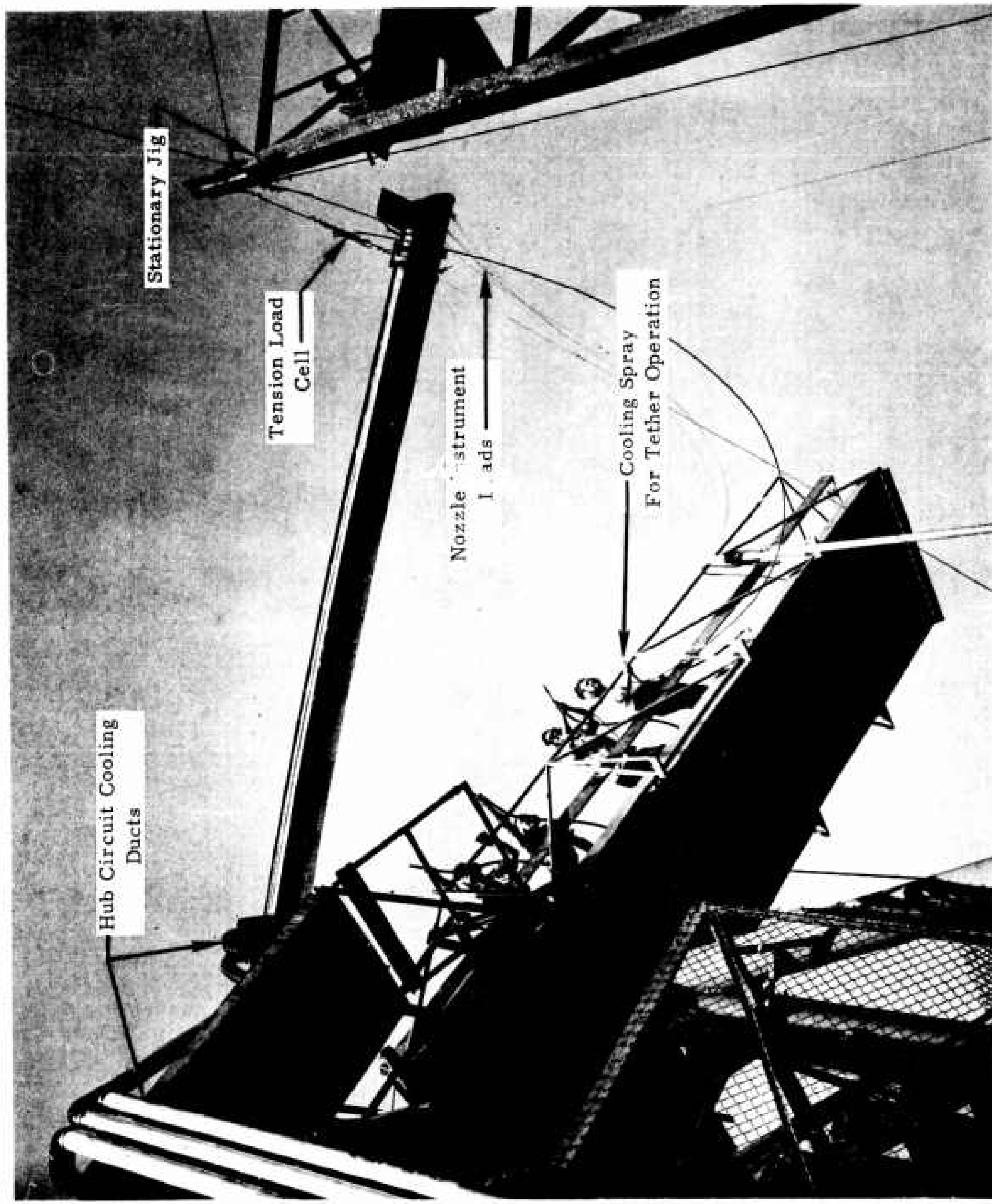

Figure 4. Thrust Tested Blade in Tethered Position

TABLE 2

TIP NOZZLE THRUST AND FLOW DATA FOR TETHER TEST

					Leading Edge Duct			Trailing Edge Duct				
1	2	3	4	5	6	7	8	9	10	11	12	13
Run	P_{t_7}	T_{t_7}	$P_{t_{Hub}}$	$T_{t_{fs}}$ *	$P_{t_{max\ nozz}}$ †	$T_{t_{nozz}}$	W_{nozz}	$P_{t_{max\ nozz}}$	$T_{t_{nozz}}$	W_{nozz}	W_{H_2O} ††	F_g
#	psia	°F	psia	°F	psia	°F	#/sec	psia	°F	#/sec	#/sec	#
1	22.20	688	20.81	558	18.86	558	4.06	19.33	558	4.42	0	205
2	24.01	782	22.64	632	20.20	630	4.46	20.81	635	4.83	0	293
3	26.21	850	24.57	720	21.59	720	3.93	22.28	720	5.07	0	353
4	27.71	910	26.16	770	22.85	770	5.38	23.63	770	5.13	0	428
5	29.21	950	27.41	605	23.95	600	6.15	24.74	610	6.32	1.02	468
6	31.61	1035	29.54	602	25.87	600	6.52	26.60	605	6.93	1.08	553
7	33.71	1025	31.55	608	27.42	608	6.55	28.26	608	7.63	1.11	607
8	34.41	1060	32.49	610	28.38	612	7.49	29.15	608	7.78	1.26	646
9	34.61	1120	32.49	690	28.37	690	7.20	29.21	690	7.43	1.08	663
10	32.19	995			26.01	670	***	26.89	660		1.00	592
11	29.44	930			22.96	665		23.90	665		0.98	530
12	34.34	1090			26.48	690		27.47	690		1.05	673
13	34.58	1100	32.53	757	26.58	730		27.81	733		1.02	683
14	34.58	1090	32.47	805	26.62	775		27.85	780		0.98	684
15	31.49	1025			24.02	755		25.15	755		0.98	594
16	31.49	1025			24.22	720		25.27	720		1.00	593
17	31.49	1035			24.47	690		25.54	690		1.02	585
18	30.06	955			24.37	675		25.25	680		0.99	549
19	30.31	960			24.56	720		25.40	720		†††	549
20	30.40	965			24.56	765		25.59	765		†††	545
21	27.75	880			22.42	675		23.28	675		†††	459
22	27.75	880			22.40	710		23.28	710		†††	462
23	34.23	1100	32.20	799	**						0.99	695
24	34.42	1100	32.44	751							1.30	693
25	34.37	1100	32.39	688							1.10	696
26	34.62	1100	32.63	603							1.25	702
27	25.83	900	24.22	740							0	411

* The subscript fs pertains to the flow measuring station where $T_{t_{fs}} \approx T_{t_{hub}}$ (mass weighted).
Note that the values of Columns 7 and 10 are sometimes greater than 5, indicating blade temperature losses smaller than instrument accuracy.

** Nozzle instrumentation removed for these runs.

*** Static pressure probe began to leak and provided erroneous data.

† Max. corresponds to maximum velocity at duct center.

†† W_{H_2O} total cooling water injection rate. This value is included in the sum of 8 and 11.

††† Water flow rates were below calibration reliability (0.98 #/sec) of the flow meter.

10 X 10 TO THE 1/2 INCH 359-11
KEUFFEL & ESSER CO.

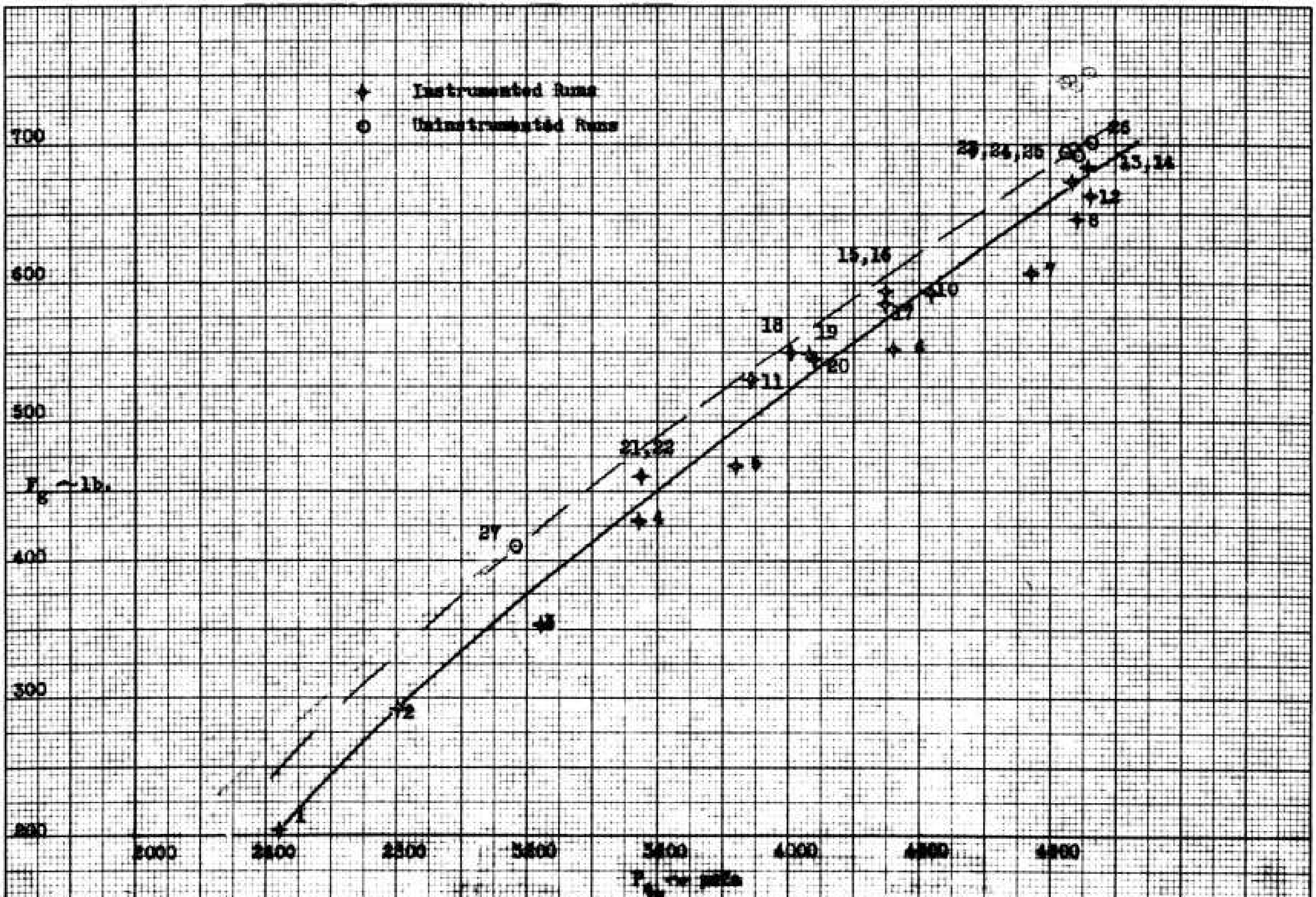

Figure 5 Comparison of Rotor Tip Thrust as a Function of Turbine Discharge Pressure with and without Nozzle Probes Installed.

4. NOZZLE PARAMETERS

The tether test partially described in Section 3 provided data to establish nozzle coefficients, thereby allowing a check on previous estimates. Pressure and temperature instrumentation (P_t, P and T_t) was provided in the leading and trailing edge primary flow ducts of the blade tested (Figure 6). The position of these instruments was 2 to 3 hydraulic diameters upstream of the nozzle inlet and it is assumed herein that the loss in total pressure and temperature was negligible between the plane of measurement and the nozzle inlet.

Total pressure probes were centered in each duct to establish the maximum velocity head, and the method established in Section 10 was used to determine flow rate and mass - weighted nozzle inlet total pressure. The center of pressure for the nozzle exhaust was estimated to be at Station 329.5 R.

Only a few test runs provided adequate data required to determine nozzle parameters. For the reason described in Section 3, nozzle instrumentation was installed for Runs 1 through 22 and was removed for Runs 23 - 27. During Run 10, the leading edge duct nozzle inlet static pressure probe began leaking. Runs were continued at high turbine discharge pressure values since for nozzle choked conditions, a knowledge of nozzle inlet total pressure and a previous fix on nozzle inlet Mach number establishes the flow rate when changed R, γ, and area effects are negligible. During the analysis, for Runs 10 through 24 and 27 it was found that although the total pressure at the center of the duct indicated a nozzle pressure ratio above the choked value in many cases, the mass weighted mean total pressure was inadequate for choking in any of these runs. The unchoked condition then does not provide a constant nozzle inlet Mach number and thus the $P_{t_{nozz}}$ values are insufficient to determine flow rate. It was found that the low total pressure values at the nozzle were due to high duct losses as explained in Section 2.

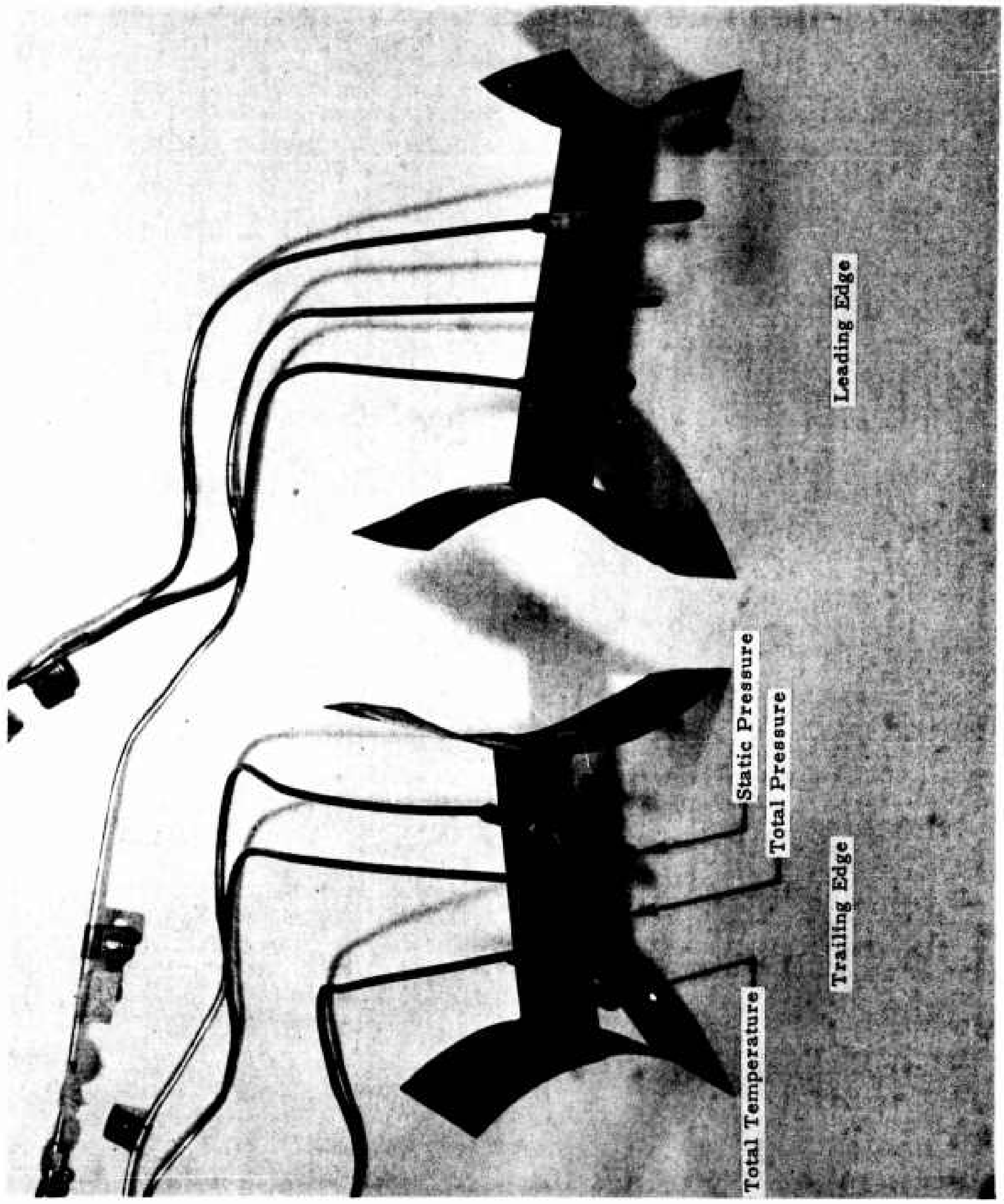

Figure 6. Nozzle Inlet Station Temperature and Pressure Probes Temporarily Installed for Tether Test

A second check on the flow rates is afforded by the values determined at the stack flow measuring stations discussed in Section 10. The flow rates determined from these stations could have been used to estimate the blade flow rates but since Runs 10 through 24 plus 27 provided unchoked nozzle conditions, it was decided that the results of data analysis of these runs would not significantly add to the over-all picture. However, an attempt to use flow measuring station data was made in order to establish the nozzle coefficients for the choked runs (25 and 26). The effective velocity coefficients resulting were unbelievably high and are thus not presented. This discrepancy is attributed to the effect of nozzle area change (instrument lead removal) on estimated inlet Mach number.

For the previous runs (1 through 9), there were seven unchoked and two choked cases for which redundant data at the flow measuring and nozzle inlet stations were taken. This, then, provides flow data measured at stations in series and establishes the adequacy of using Nikuradse's data (Reference 1) to measure the flow at the two parallel stack flow measuring stations as accomplished in Section 10. Except for Run 3 (Table 3, Column 34) which indicated an error of + 18.6% between the flow station measured rates and nozzle inlet station measured rates, the maximum flow measurement error for the other runs was

$$\%\ \text{error} = \frac{\text{Flow Meas. Stat. Flow} - \text{Nozz. Stat. Flow}}{\text{Flow Meas. Stat. Flow}} \times 100 = 10.8\%$$

while for the two instrumented choked runs the maximum error was + 2.4% (based on 1st iteration, see Section 10.1).

In order to correlate the data to provide the coefficient corrections due to instrument blockage a plot of thrust with and without instrumentation must be analyzed. A study of Figure 5 indicates that in the choked region, the thrust increase without blockage was approximately 25 lbs. The percentage of thrust increase varies from about 4% in the choked region to more than 20% at low turbine discharge pressure. Since instrumented and uninstrumented runs are compared on the plot at identical gas generator and duct conditions, the increase in gross thrust (ΔF_g) in terms of percent corresponds to identical increase in thrust coefficient (ΔC_f). In this manner the relation between thrust coefficient as a function of NPR for uninstrumented runs can be established as shown in Figure 7b. To determine velocity and flow coefficients in similar terms a relation from Section 11 is used:

$$C_f = C_{vf} \times C_w , \tag{1}$$

and

$$(C_f + \Delta C_f) = (C_{vf} + \Delta C_{vf})(C_w + \Delta C_w). \tag{2}$$

It is seen that the percentage effect of ΔC_f caused by C_{vf} and ΔC_w can be found only if the relationships between ΔC_{vf} and ΔC_w are known. The data taken during the tether test does not provide this relationship. However, since the change in flow coefficient (ΔC_w) is directly affected by the flow rate while the effective velocity coefficient is affected by the square root of the flow rate, only slight error is involved when assuming

$$\Delta C_w = 2 \Delta C_{vf}. \tag{3}$$

Equation (3), then, provides the additional relationship enabling a solution of Equation (2). However, the function of C_{vf} vs NPR for uninstrumented runs can be determined in two slightly different ways. First, by correcting the second iteration at one point in the choked region where the function C_{vf} is almost constant, and, completing the curve graphically using the existing plot as a guide. For this purpose, in the following calculations the choke point at NPR = 1.86, was selected.

The other solution is obtained by applying Equations (2) and (3) over the entire range of NPR. The redundant plot can serve as means of checking the relationship between all three parameters. Originally, the first approach was used to establish the velocity coefficient (recommended) on Figure 7a, then from Equation (1) C_w (recommended) was determined on Figure 7c. Comparing the two figures it can be seen that $\Delta C_w = 2\Delta C_{vf}$ which means that the results from two methods coincide with good accuracy. Incidentally the recommended velocity coefficient C_{vf} is in close agreement with the results of many investigations made in this field. Generally, the velocity coefficient is not much affected by different nozzle shapes, methods of contraction or changes in convergence angle.

Following the first approach at NPR = 1.86, from Figure 7a, 7b and 7c at NPR = 1.86

$C_f = 0.888$, $\Delta C_f = 0.031$

$C_{vf} = 0.968$

$C_w = 0.919$

Substitution in equation (2) yields

$$(0.888 + 0.031) = (0.968 + \Delta C_{vf}) (0.919 + 2 \Delta C_{vf})$$

from which

$$\Delta C_{vf} = 0.01$$

This correction was applied to the second iteration value (measured coefficients for blocked nozzle) of Figure 7 at NPR = 1.86 to provide the recommended nozzle coefficient.

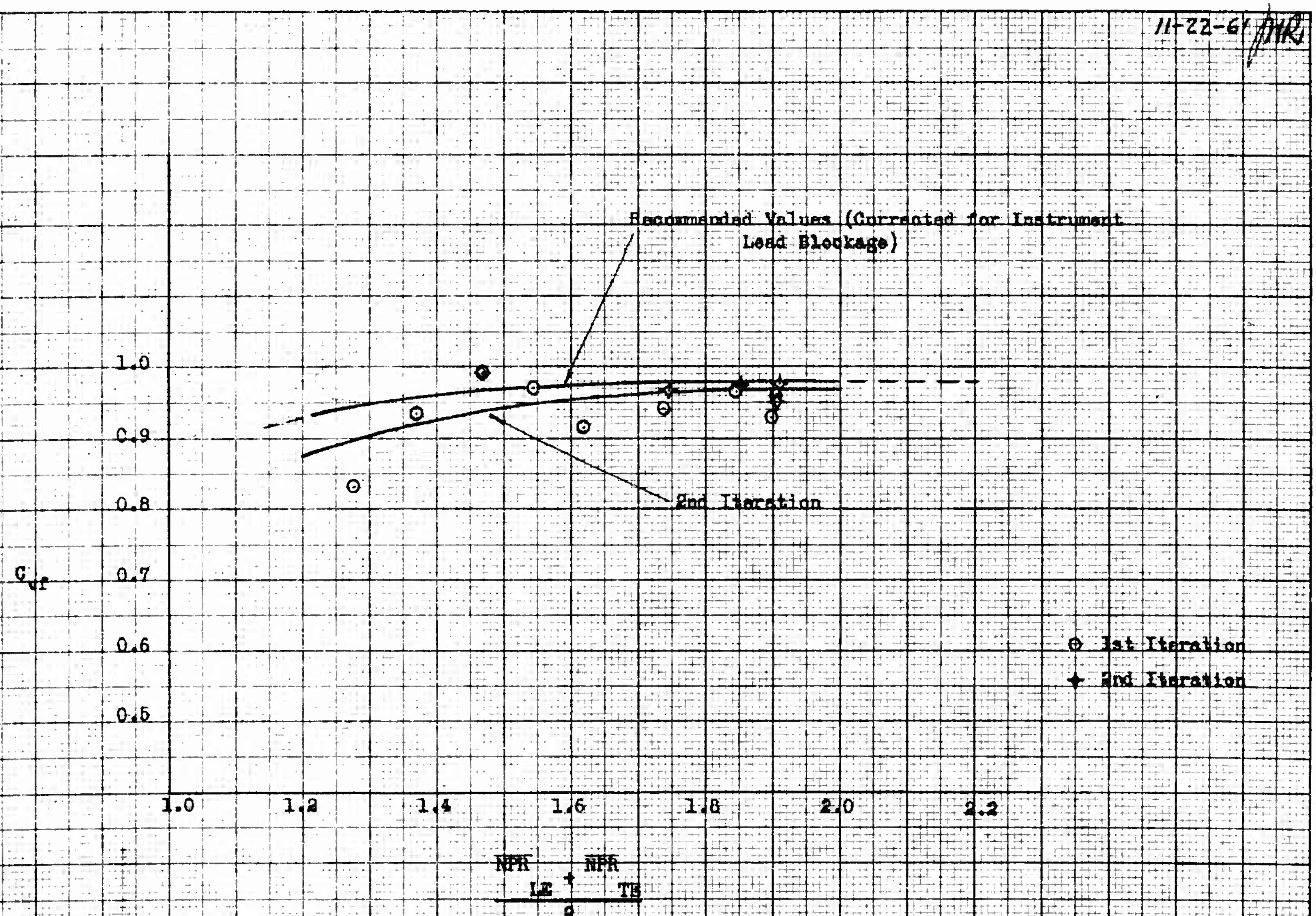

FIGURE 7.8

NOZZLE EFFECTIVE VELOCITY COEFFICIENT

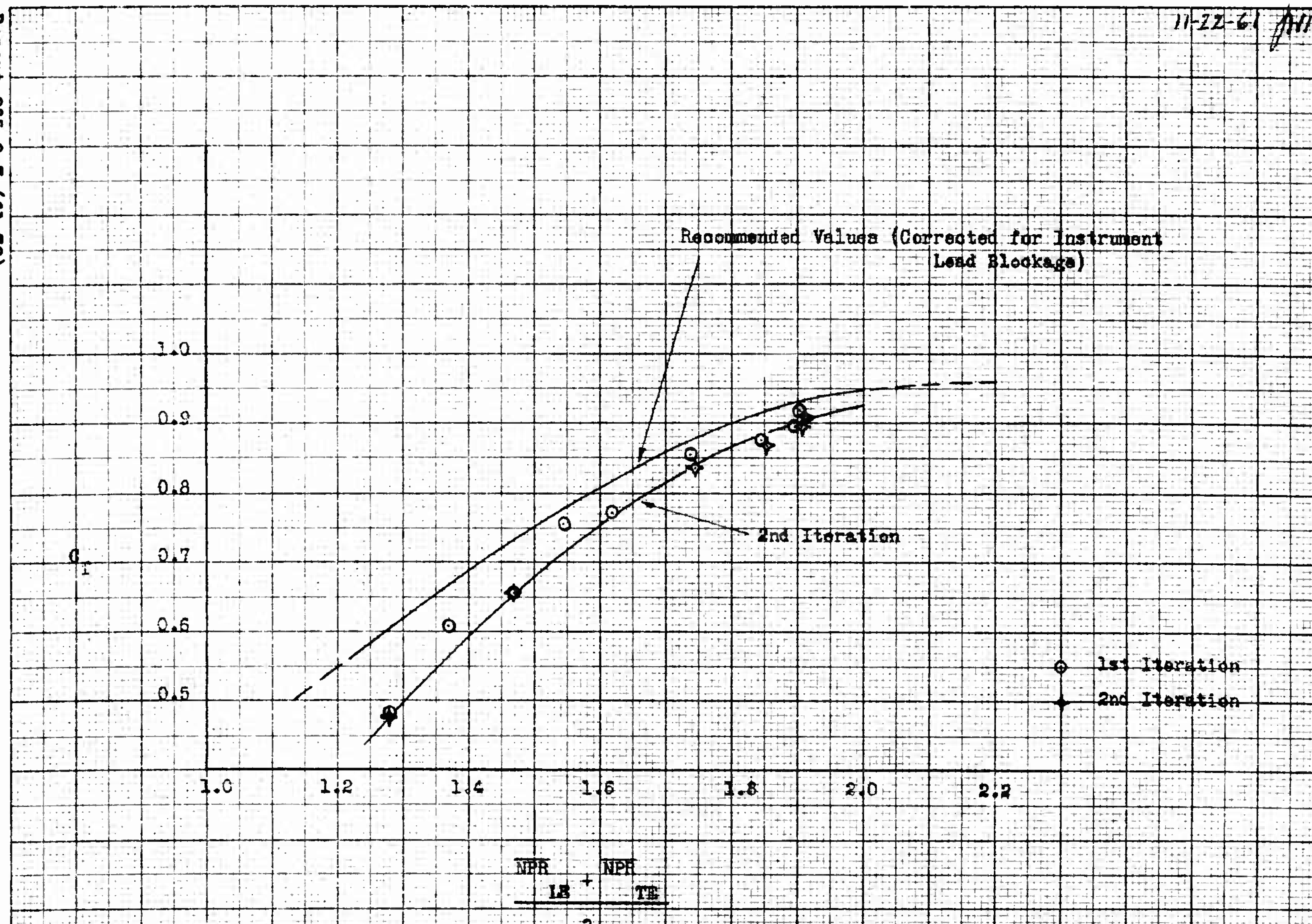

FIGURE 7.6
NOZZLE THRUST COEFFICIENT

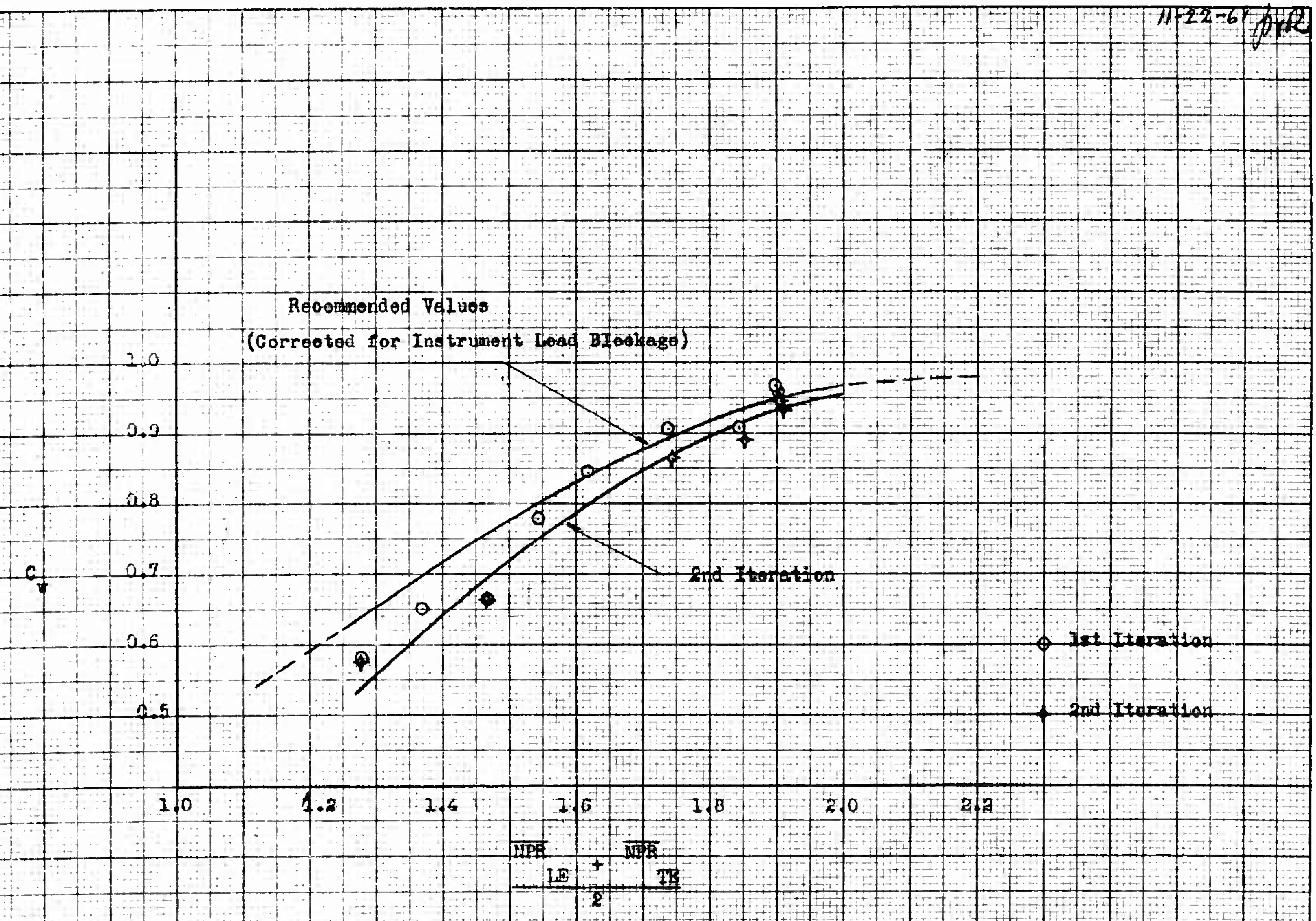

Figure 7.c. Nozzle Flow Coefficient

From Figures 7a, b, and c, which correspond to a non-rotating blade, it is seen that the effect of nozzle pressure ratio on nozzle coefficients diminishes with increasing pressure ratio. In fact, at pressure ratios above 2, the coefficients are virtually unchanged. For a whirling blade and similar engine conditions, the major blade centrifugal pumping effect is a higher nozzle pressure ratio than those measured statically and therefore corresponds to nozzle coefficients at a level indicated by the dashed lines in Figure 7.

Two additional causes produce higher nozzle pressure ratios than those measured statically. First, the maximum engine pressure ratio of the T64 (engine for flight system) is 2.8 versus 2.5 for the whirl test J57 engine; and second, the whirling aerodynamically loaded rotor produces a tip vortex which lowers the local external back pressure causing a higher nozzle pressure ratio than if the whirling blade were unloaded (i.e. no tip vortex due to lift). All of these effects produce higher nozzle pressure ratios in a region where the effect of pressure ratio on nozzle coefficients is small.

5. HUB COOLING PATH FLOW CHARACTERISTICS

The hub area is cooled by induced air flow due to centrifugal pumping (Figure 8). To determine the adequacy of the ejection ports and to ascertain the pressure loss characteristics of this path as a function of flow rate, ducts were connected to the exhaust ports (Figure 9) and a blower was provided to suck air through the hub circuit. The pressure loss was measured from ambient to a station several diameters forward of flow measuring orifices (Figure 10). With the ducts disconnected from the blade while maintaining the same flexible duct shapes, the pressure loss from ambient to the same station forward of the orifice was measured. The difference between the two pressure drops corrected by deviations from the flight flow circuit then provided the pressure loss of the hub path as a function of flow rate. This pressure loss when balanced with the centrifugal pressure rise establishes the hub circuit flow rate as a function of rotor rpm or tip speed.

Extrapolation of the flow data for rates in excess of 0.4 lb/sec was necessary due to blower limitations. For flow rates below this value, the data provided $\Delta P_t/q$ vs w values which were sufficiently constant to allow extrapolation.

For incompressible flow, the rate of change of momentum of a mass segment due to centrifugal forces is (Reference 2),

$$\rho \, v \, d \, v = \frac{V_T^2 \, \rho \, r \, d \, r}{L^2} . \tag{1}$$

Over the radial length $(r_2 - r_1)$ of the circuit, Equation (1) integrates to

$$q_2 - q_1 = \frac{\rho \, V_T^2}{2 \, g \, L^2} \left(r_2^2 - r_1^2 \right) . \tag{2}$$

With an atmospheric intake and exhaust

$$\left. \begin{aligned} P_{amb} = P_{t_1} &= P_1 + q_1 \\ P_{t_2} &= P_{amb} + q_2 . \end{aligned} \right\} \tag{3}$$

Thus, from Equations (3),

$$\Delta P_{t_{cf}} = P_{t_2} - P_{t_1} = P_{amb} + q_2 - P_1 - q_1 = q_2 , \tag{4}$$

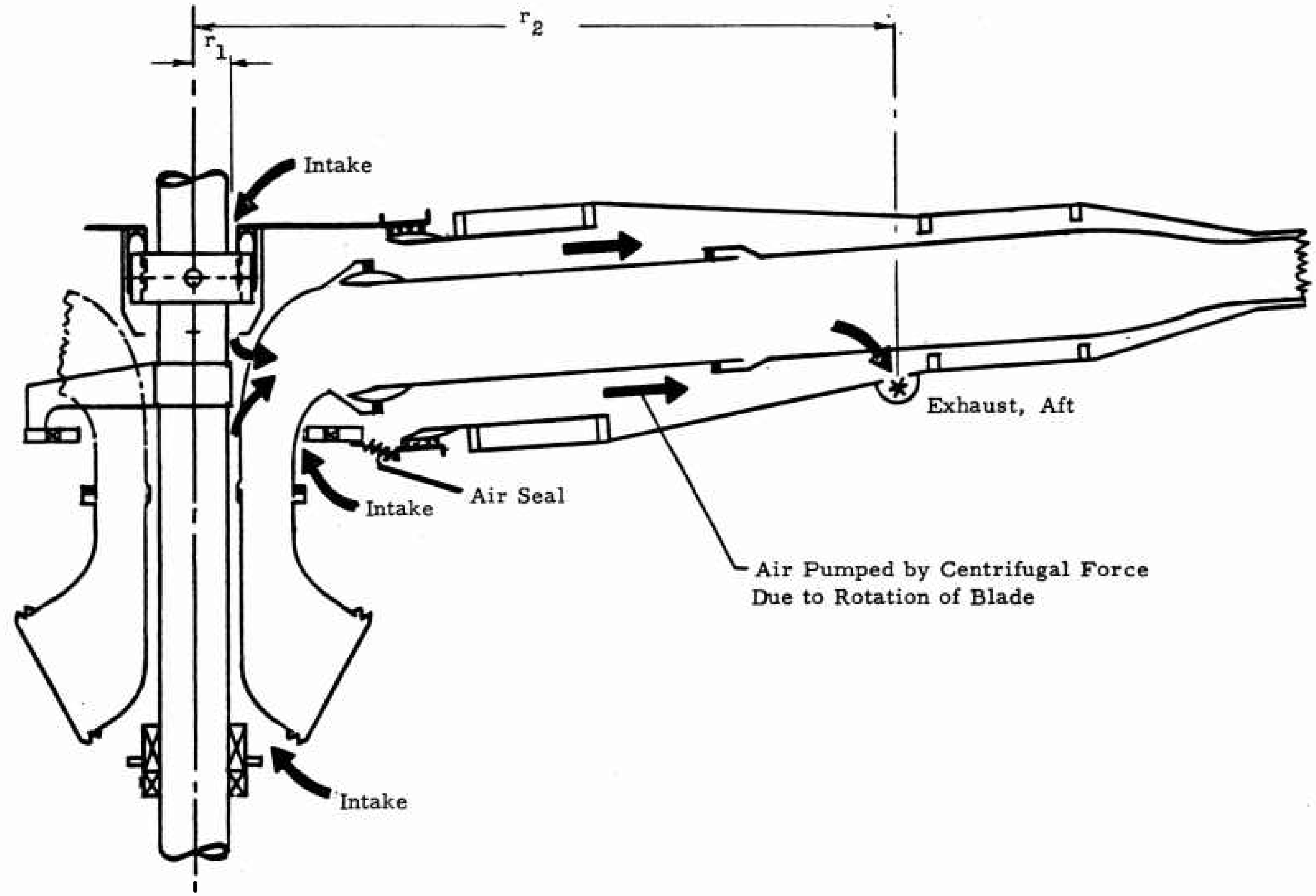

Figure 8. Schematic of Cooling System for Hub and Blade Root Components

Figure 9. Typical Flexible Couplings Attached to Blades for Tether Operation and Hub Cooling Calibration

Figure 10. Hub Cooling Blower Arrangement

and combining Equations (2) and (4)

$$\Delta P_{t_{o_f}} = q_1 + \frac{\rho V_T^2}{2 g L^2} \left(r_2^{\,2} - r_1^{\,2} \right). \tag{5}$$

Now, since the hub circuit inflow is near the rotor axis, $r_1 \approx 0$ and due to the large inlet area $q_1 \approx o$. For the hub then, Equation (5) simplifies to

$$\Delta P_{t_{o_f}} \approx \frac{\rho V_T^2 r_2^2}{2 g L^2} = \frac{r_2^2 \; V_T^2 \delta}{288 \; g \; L^2 R \theta} \times \frac{14.7}{519} . \tag{6}$$

The air is exhausted through five ports of varying area at different radii from the hub centerline. The mass flow through a number of exhaust holes can be represented by

$$w_{tot} = \sum_n w_n = \sum_n C_{d_n} A_n \sqrt{\frac{\rho_n \; V_T^2 \, r_n^2}{2 \; g \; L^2}} . \tag{7}$$

Assuming the discharge coefficient C_d to be equal for each exhaust port and assuming incompressible flow, Equation (7) may be written as

$$w_{tot} = C_d \, A_{tot} \sqrt{\frac{\rho \; V_T^2 \, r_{eff}^2}{2 \; g \; L^2}} = \sum_n C_{d_n} A_n \sqrt{\frac{\rho_n \; V_T^2 \; r_n^2}{2 \; g \; L^2}} ,$$

from which an effective radius based on total discharge area may be defined as

$$r_{eff} = \frac{\sum_n A_n \; r_n}{A_{tot}} . \tag{9}$$

Substituting this value of r_{eff} for r_2 in Equation (6) and utilizing the test data previously described results in the nomographic plot of ΔP_{cf} vs $\frac{V_T \sqrt{\delta}}{\sqrt{\theta}}$ and $\Delta P_{t_{sm}}$ (statically measured) vs $\frac{w\sqrt{\theta}}{\delta}$ as presented in Figure 11. From this figure, the hub cooling flow rate as a function of altitude ambient conditions and rotor tip velocity is quickly ascertained. For sea-level standard-day conditions, it is seen that the required flow rate of approximately 1 lb/sec per blade as assumed in previous thermal analyses is achieved.

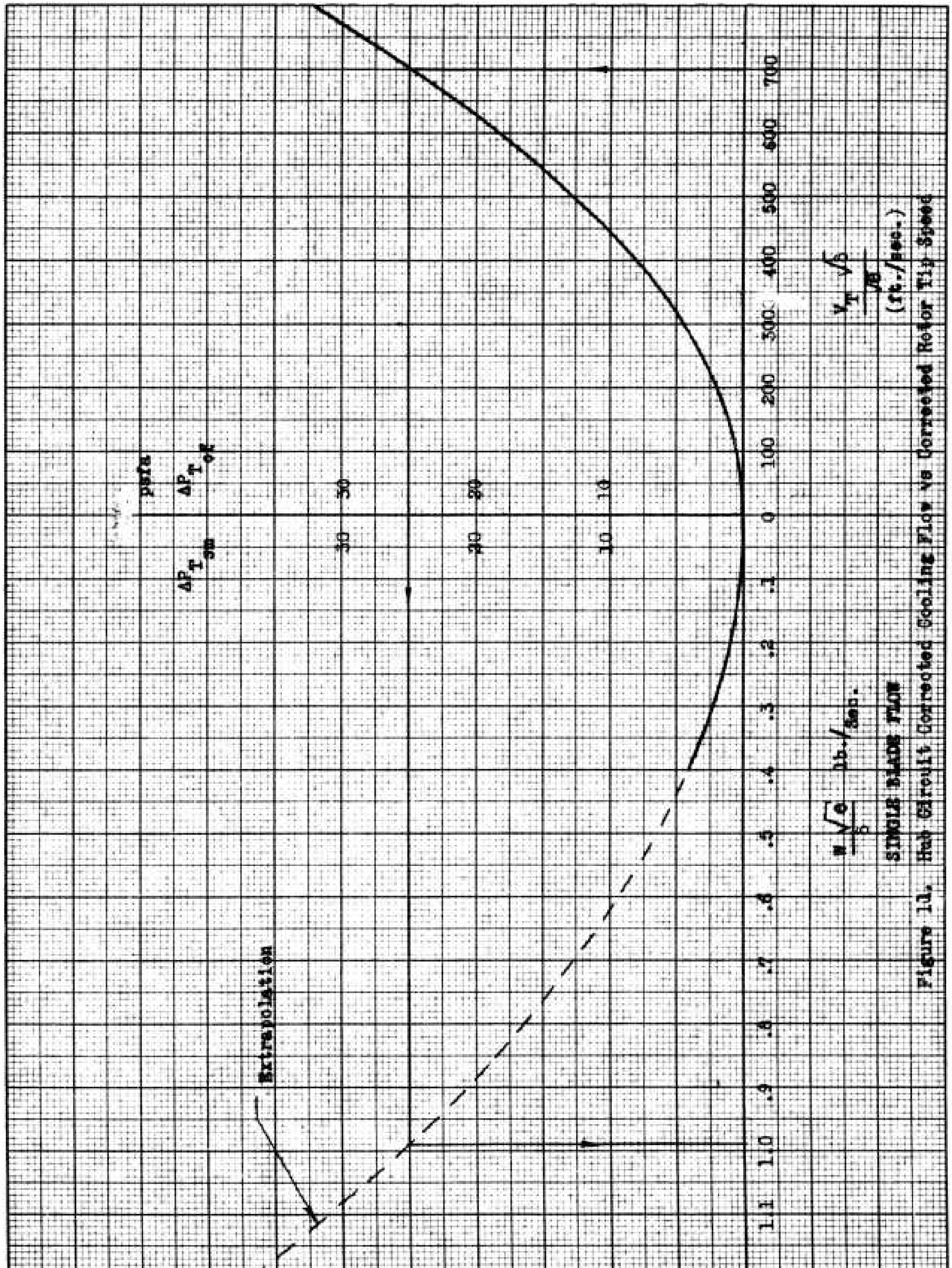

Figure 11. Hub Circuit Corrected Cooling Flow vs Corrected Rotor Tip Speed

6. GAS GENERATOR INSTALLATION AND OPERATING CHARACTERISTICS

The J57-P-19W turbojet engine was selected as the whirl test gas generator since it is the most reliable engine currently available that suitably approximates the turbine discharge conditions of the T64 engine proposed for the Hot Cycle Helicopter. The large differences in air flow between these engines is accommodated by dumping approximately 60% of the J57 exhaust gas through a butterfly valve which also serves as a means of varying the engine operating line to achieve planned test conditions.

6.1 Installation

The J57 is installed at the base of the whirl test stand as shown in Figure 12. The reversibility of the engine mounting structure facilitated the initial power plant operation for familiarization and gas generator calibration with the standard turbojet nozzle. Approximately one-third of the hot gas from the J57 is removed from the main exhaust duct and directed into the rotor blades through a vertical duct system in which the gas temperature and pressure distribution is accurately measured. The unused engine exhaust is ducted aft where a butterfly dump valve controls the pressure within the system.

Normal installation practices are adhered to as detailed in Reference 3. While the whirl test engine installation is considered to be such that sufficient external engine cooling could be obtained for normal engine operation, temperature sensors of prototype installation type (Reference 3) are utilized due to projected operation above the normal engine operating line.

During the planned series of tests, considerable operation is to be conducted at very low engine power settings, especially during the initial whirl tests. The engine fuel flow which normally acts as the means of removing heat from the engine oil is not great enough to avoid over-temperature of the oil during prolonged

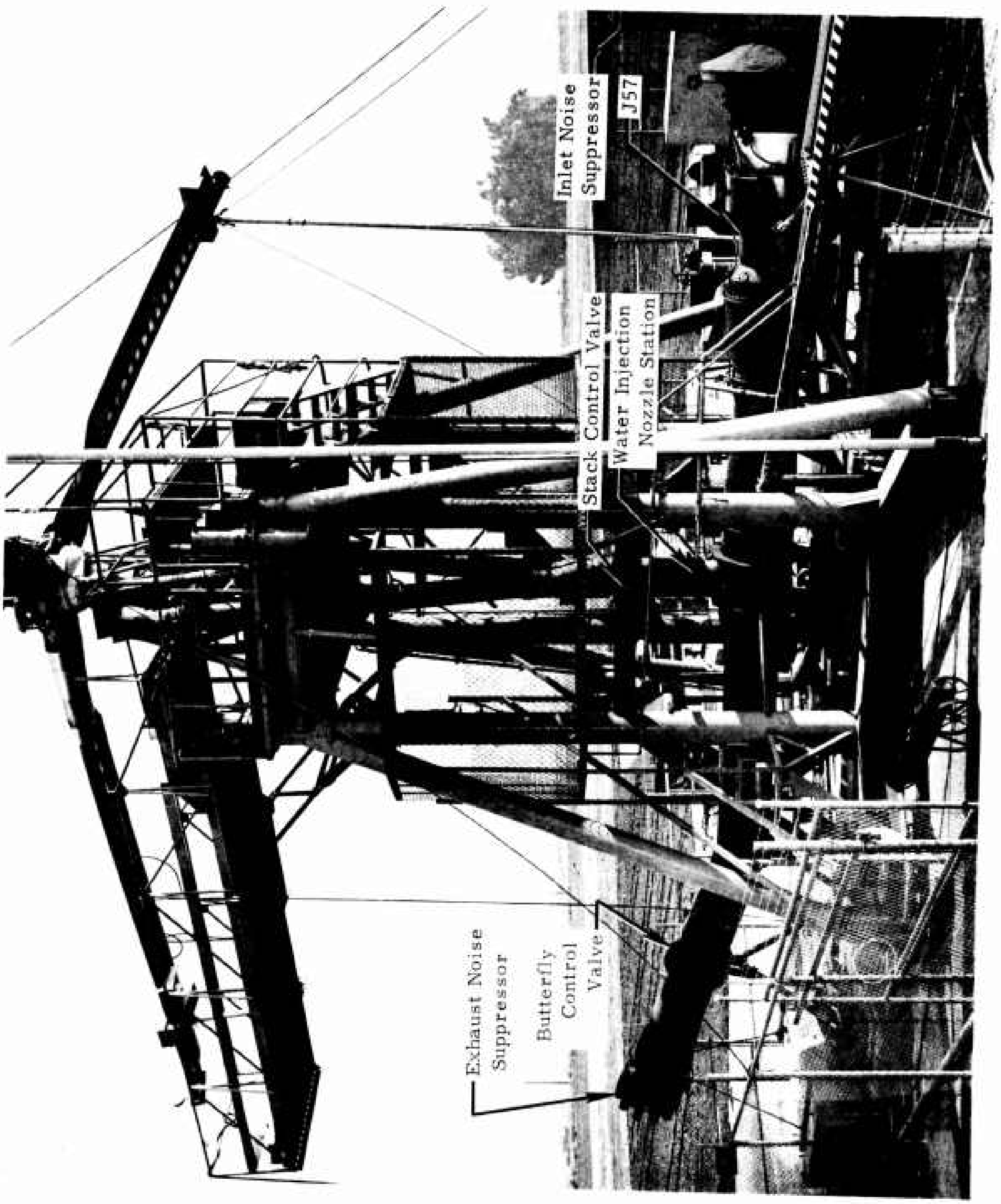

Figure 12,a. J57 Gas Generator Installation operation of this type. For this reason, a pair of hydraulically driven engine oil-to-air coolers is utilized (Figure 12).

Engine throttle control is maintained from the mobile control van by a hydraulic servomechanism located on the blade collective pitch stick. Emergency throttle cut-off is available instantly through the use of a hydraulic accumulator which discharges high pressure fluid into the throttle servo when electrically actuated.

6.2 Initial Operation and Calibration

The first engine operation was conducted on May 17, 1961 in the presence of Pratt and Whitney Service Corporation personnel. Operator familiarization was completed at that time.

The engine calibration was conducted to determine the normal engine operating line with the standard jet nozzle. This was done to avoid deviations from normal engine operation during transients when the J57 gas generator is connected to the Hot Cycle test system. Figure 13 shows the engine installed in the calibration position with the direction of flow reversed 180° from the normal whirl test position.

Complete engine operation data were obtained and all external temperatures were monitored. The results of the engine calibration are shown in Figures 14 through 16 where turbine discharge total temperature, total pressure, and fuel flow are shown as functions of high pressure compressor rpm. The humidity correction for fuel flow is presented in Figure 17. Figure 18 which indicates the variation of turbine discharge pressure with temperature for both the J57 and T64, provides a comparison of the relative performance capabilities of the test and flight gas generators.

Since the high power operation of the J57 is limited by engine pressure and rpm, the maximum temperature, T_{t_7}, obtained during on-line operation was 1036°F.

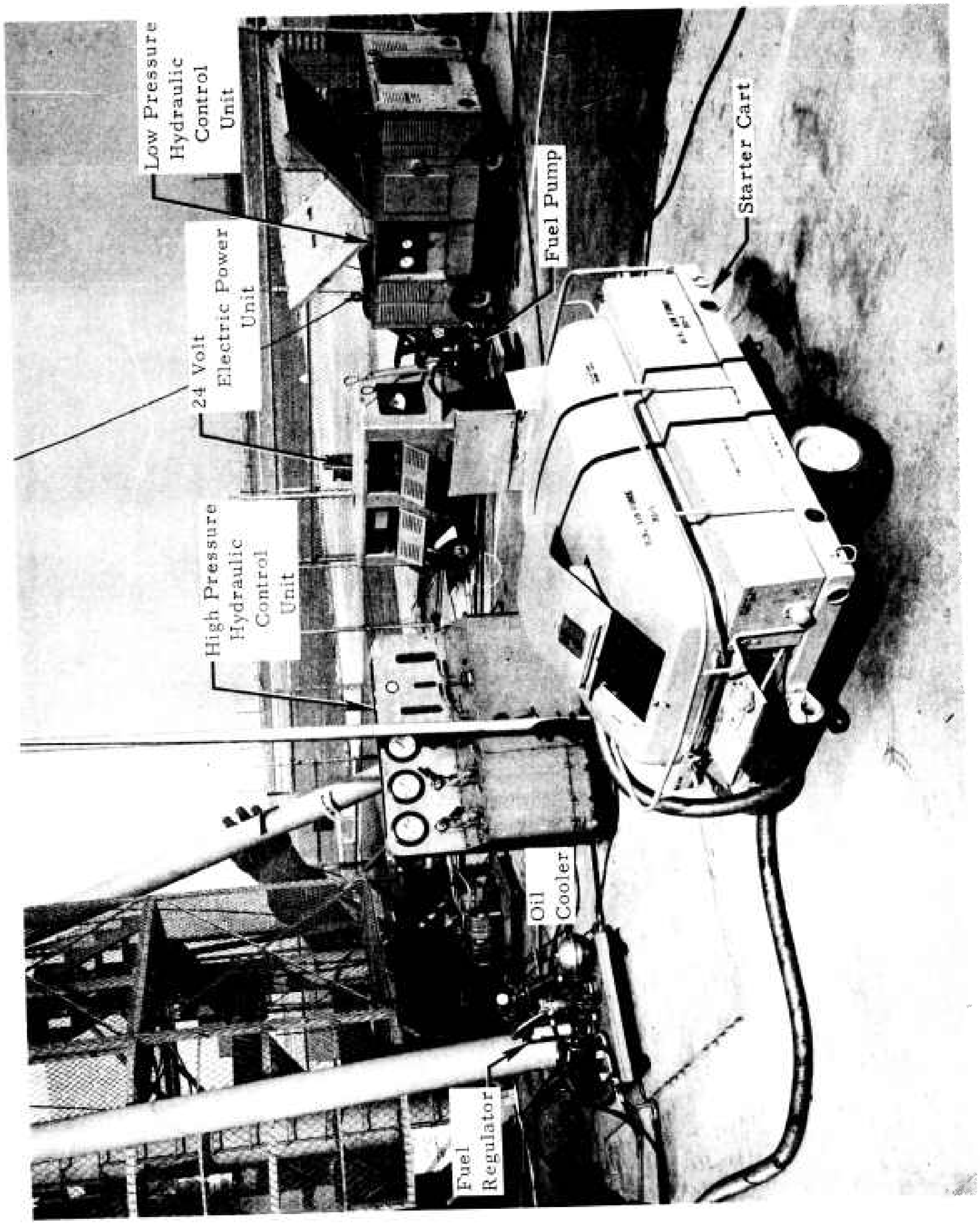

Figure 12,b. Auxiliary Power and Cooling Units for Whirl Test Installation

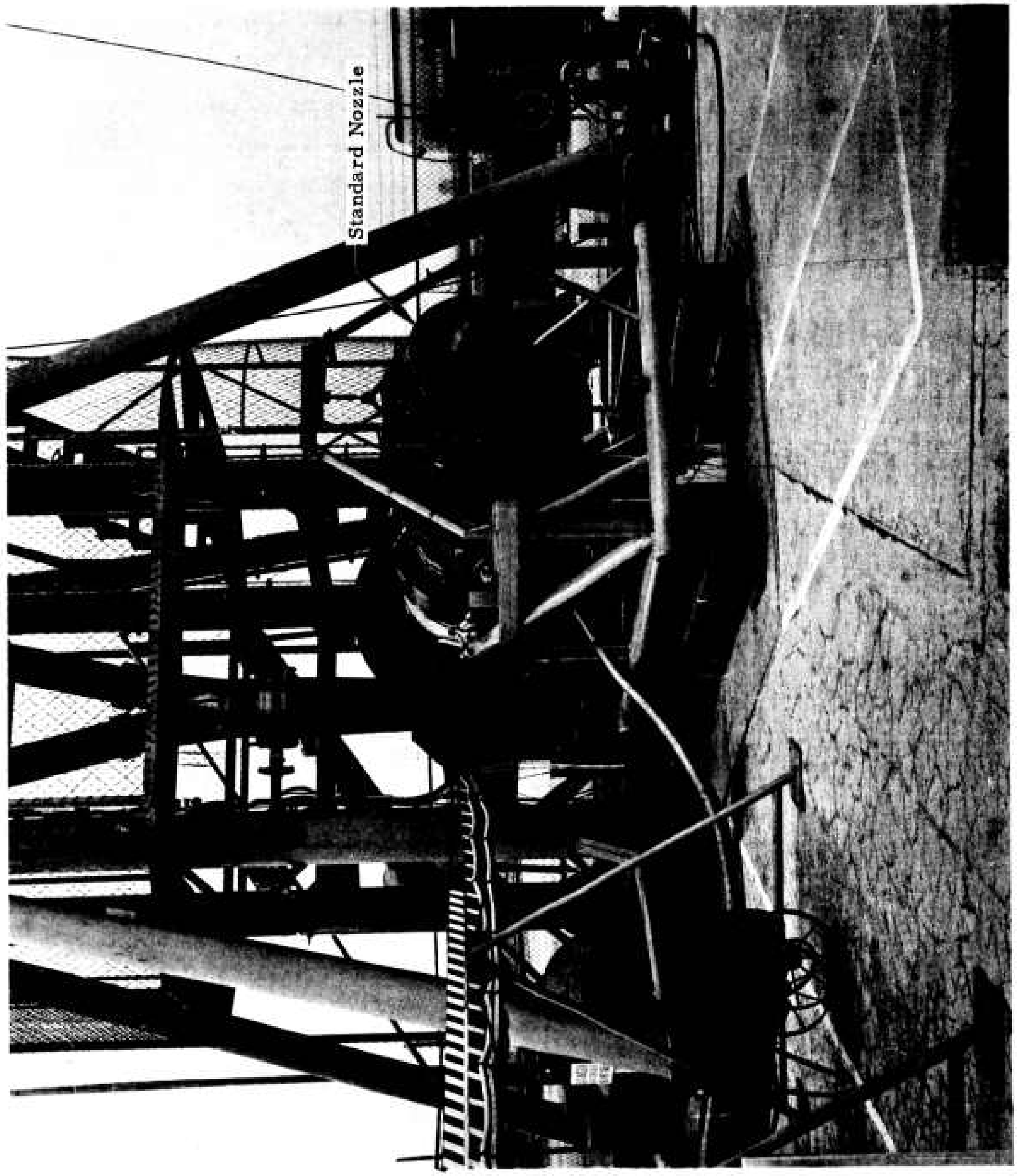

Figure 13. J57 Engine in Calibration Position

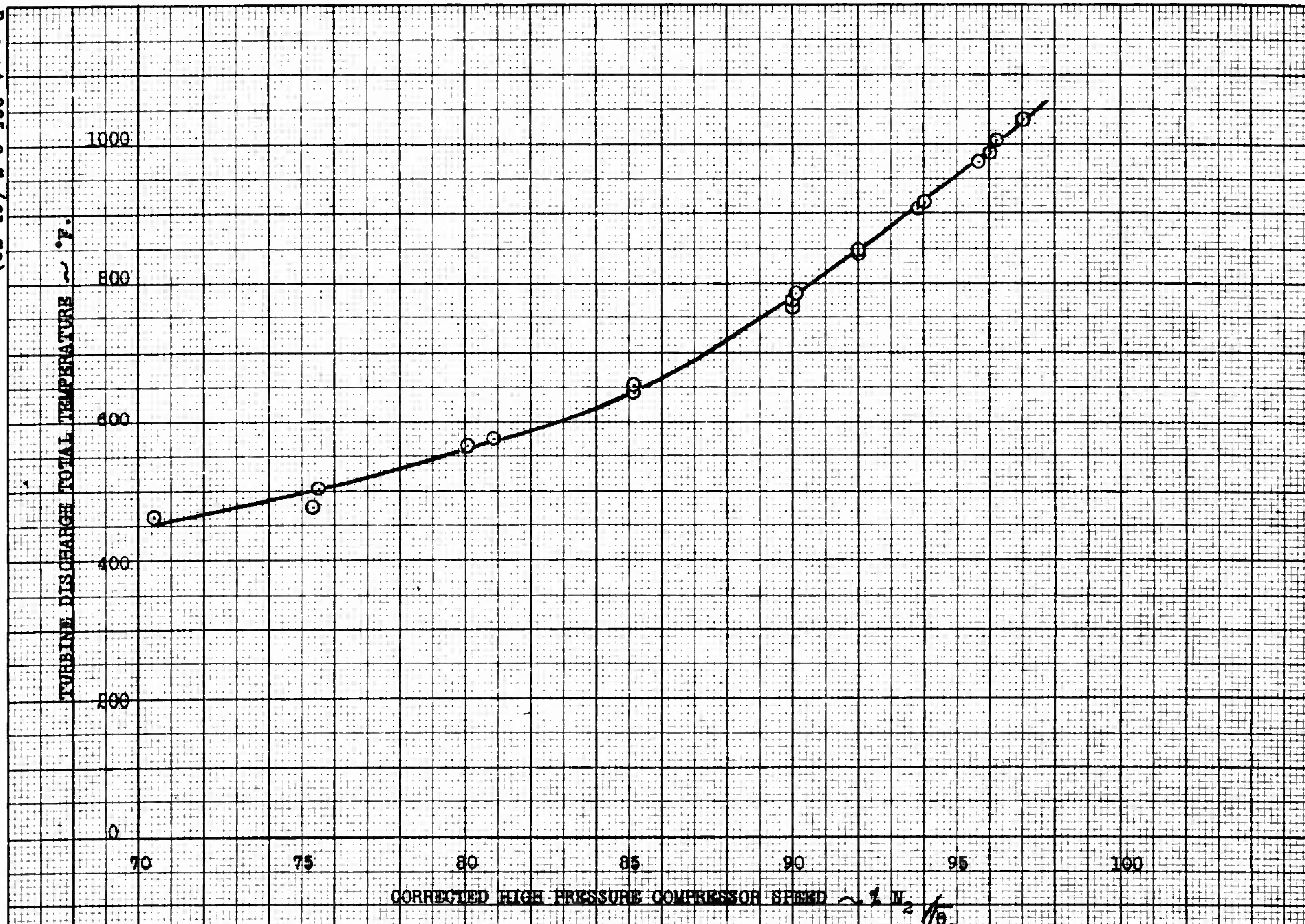

Figure 14. J57-P-19W Engine Calibration; 63° Ambient Temperature

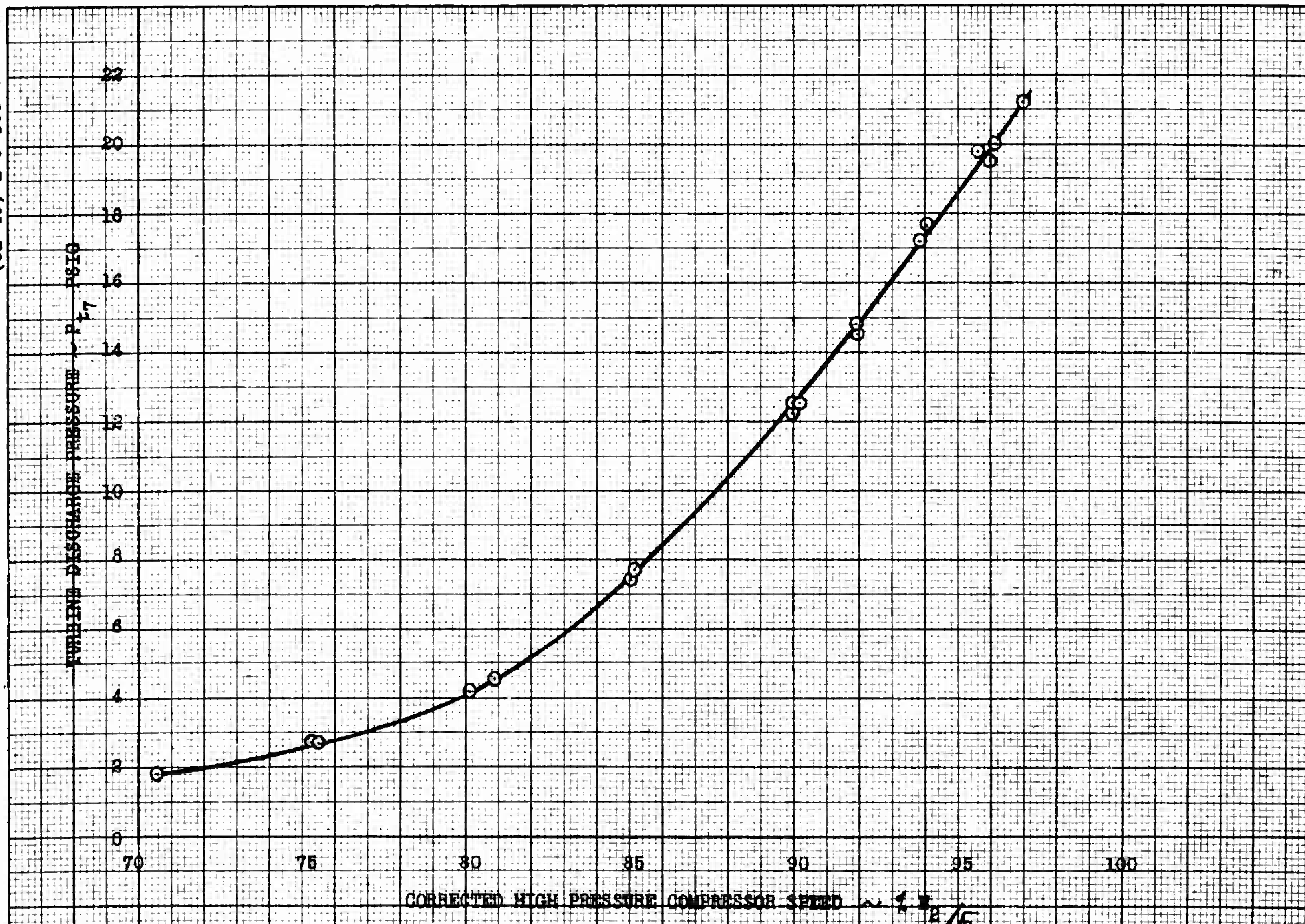

Figure 15. J57-P-19W Engine Calibration; 63°F. Ambient Temperature

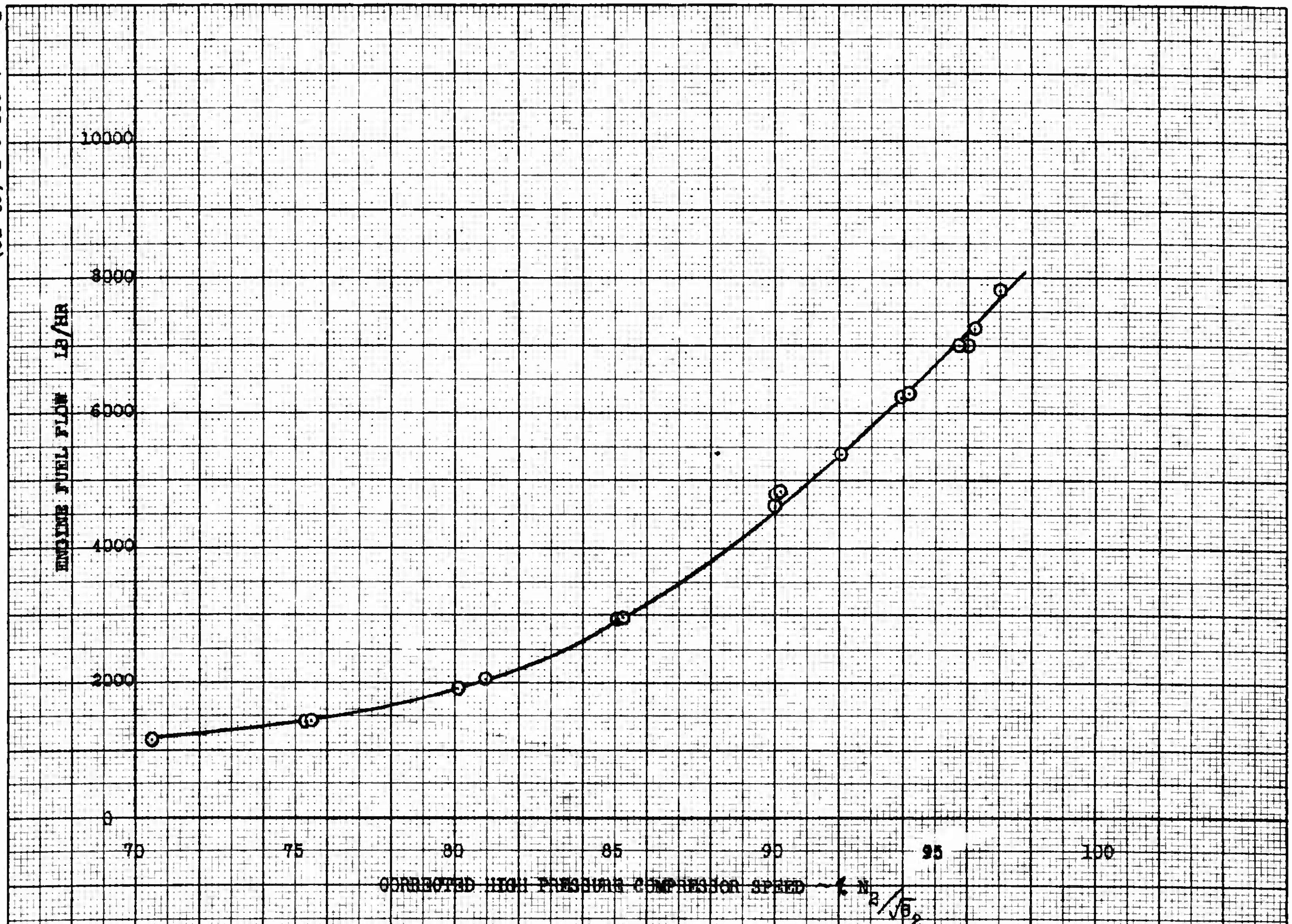

Figure 16. J57-P-19W Engine Calibration, 63°F Ambient Temperature

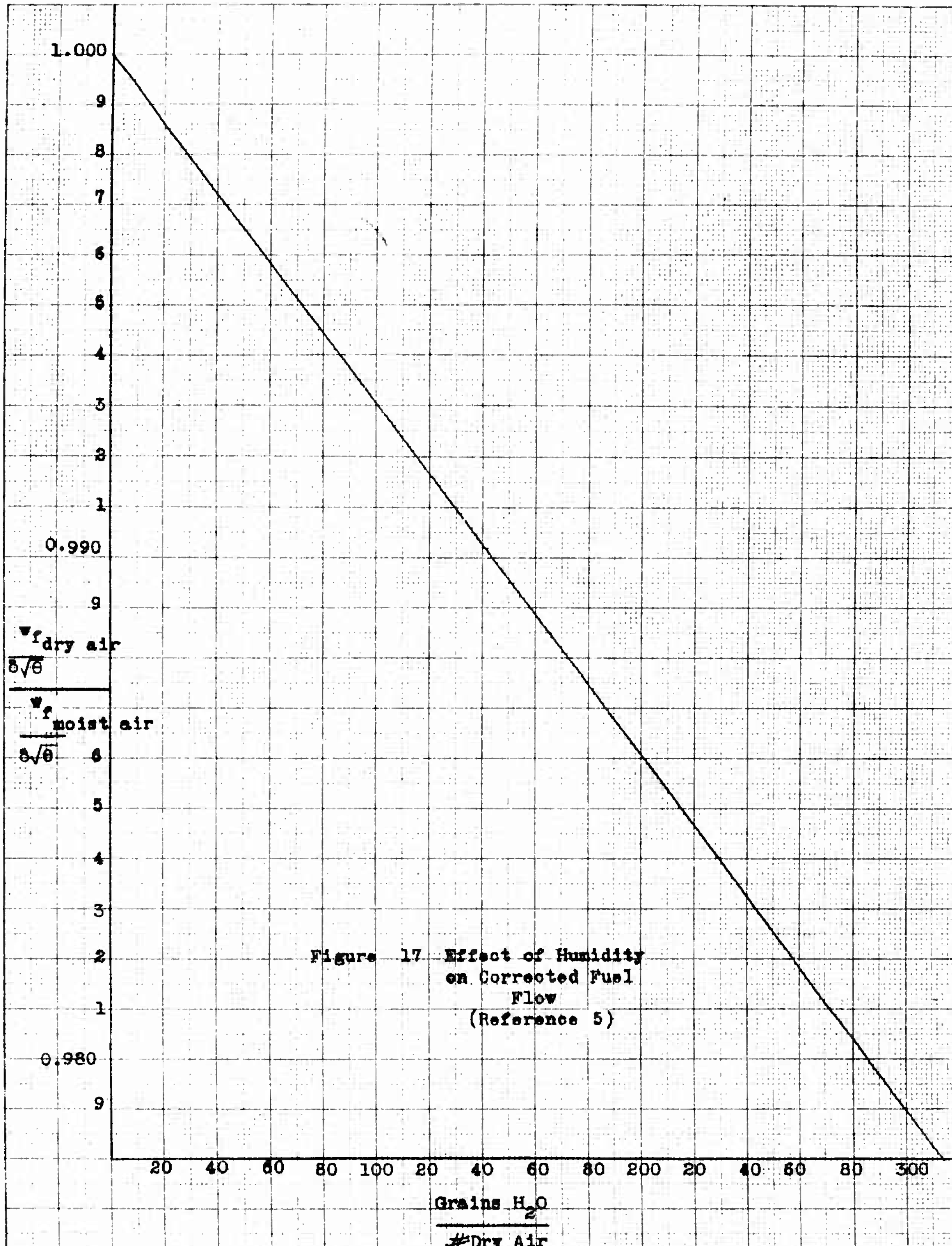

Figure 17 Effect of Humidity on Corrected Fuel Flow (Reference 5)

Report 285-9-7 (61-79)

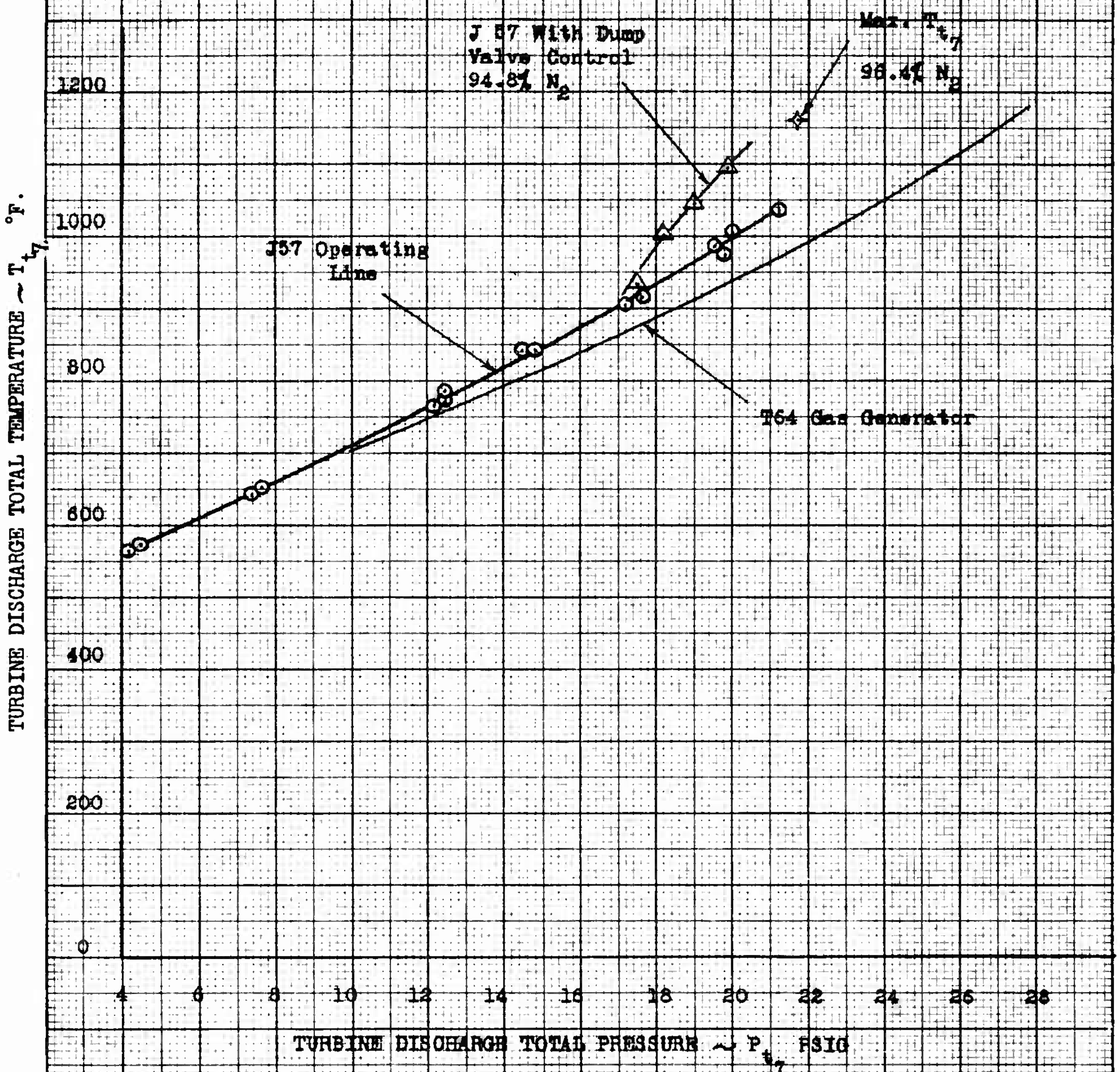

Figure 18. J57-P-19W On and Off – Line Operation Comparison with the T64

As stated earlier, however, the dump valve does provide for controlled off-line operation to achieve the required temperatures at less than maximum rpm without exceeding the engine pressure ratio limits of Reference 4.

Following the engine calibration, the J57 was installed with the jet nozzle removed and the turbine casing mated directly to the whirl test duct as shown in Figure 12. With the upper butterfly valve closed to avoid flow through the then installed rotor blades, a series of engine runs were made to determine the off-line exhaust gas temperature capabilities and the sensitivity of the engine to sudden transients initiated by rapid dump valve movement.

The variation of T_{t_7} with P_{t_7} is shown in Figure 18 for off-line operation at constant N_2. This operation was conducted above the normal operating line thereby resulting in lower than normal low pressure compressor speeds indicating a decrease in airflow due to the smaller flow area at the choked valve. Again, noting Figure 18, it is seen that the maximum turbine discharge temperature attained was 1160°F at maximum engine pressure ratio. It should be noted that this turbine discharge temperature is not considered to be the maximum obtainable since operation closer to the compressor stall line would yield a higher temperature but would possibly result in non-destructive compressor instability.

6.3 System Tests

There have been no engine difficulties encountered which have caused delays. However, a discrepancy was found between the exhaust gas temperature as measured at the turbine discharge by the engine furnished thermocouple assembly and the temperatures indicated by the flow measuring station instrumentation. This deviation is shown in Figure 19 for a limited range of temperature.

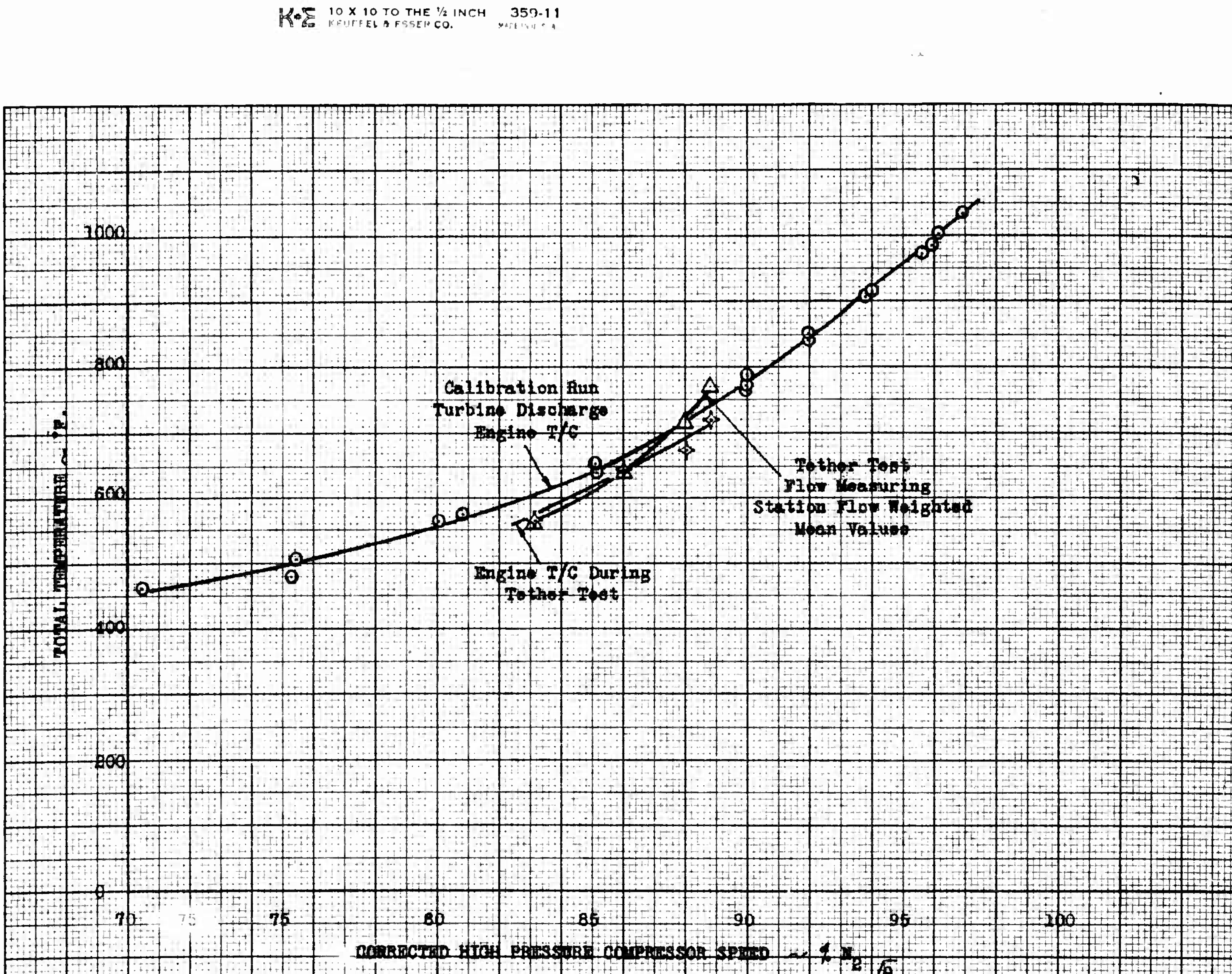

Figure 19. Comparison of Streamwise Temperature Measurements

7. SUMMARY

This report covers the analyses and experimental findings of static tests of internal flow channels of the Hot Cycle system. Pertinent results are as follows:

a. Maximum thrust recorded was 702 lb/blade (9.6% water injection, $T_{t_{nozz}} \approx 730°F$) which was consistent with the prevailing nozzle pressure ratio and gas temperature.

b. Test derived values of the tip nozzle coefficients substantiate those which were predicted and used in past performance analyses. The previously assumed effective velocity coefficient of 0.955 and flow coefficient of 0.96 were repeatedly achieved or exceeded in the near choked and choked nozzle flow ranges. At nozzle pressure ratios above 1.75 the effective velocity coefficient (C_{vf}) was found to be 0.98, and the flow coefficient (C_w) was found to be increasing from 0.935 at NPR = 1.86 to 0.98 at NPR = 2.2. Figure 7 shows the recommended values of all coefficients.

c. Primary duct pressure loss characteristics are essentially in agreement with predictions. This report covers the test period up through the tether test. Through that time, only that test provided adequately high flow rates to estimate duct losses. Unfortunately, this test provided a 3:1 unbalance of flow in the two parallel stacks. This notwithstanding, agreement between analyses and tests was observed for the stack ducts. The use of a single blade for thrust measurement yielded large pressure losses in the hub by causing flow mal-distributions (amplified secondary flow). The estimated turning losses in the hub were of the order of 4% P_{t_7} which is approximately 300% greater than the full scale model tested value (3 blades) of Reference 6 which is more realistic.

d. The pressure loss and centrifugal pumping characteristics of the hub cooling circuit were ascertained. Statically tested pressure losses when compared with calculated centrifugal pressure pumping capability of the hub circuit indicate that the provided blade cooling air ejection ports are adequate. For whirl tests at 800°F and 50% design rpm, there has been no problem with hub or spar cooling. A detailed temperature survey of the blade and hub is contained in Reference 9.

e. No problems with engine function have evolved. Turbine discharge temperature in excess of 1160°F and engine pressure ratios of 2.48 have been achieved.

f. The flow data analysis procedures have been established. Installed test instrumentation has proven satisfactory to allow correlation of analysis and test. Particularly, redundant data have yielded encouragingly similar results.

8. REFERENCES

1. Knudsen, J. G. and Katz, D. L.; "Fluid Dynamics and Heat Transfer"; McGraw-Hill Book Co., Inc., 1958.
2. Henry, J. R.; "One-Dimensional, Compressible, Viscous Flow Relations Applicable to Flow in a Ducted Helicopter Blade"; NACA Technical Note 3089, December, 1953.
3. Pratt and Whitney Aircraft; "Gas Turbine Installation Handbook, JT3 Turbojet Engines; Vol. 1"; May, 1956
4. Pratt and Whitney Aircraft; "Specific Operation Instructions J57-P-19W; Turbojet Engines"; Operation Instruction 138; July 1, 1957.
5. Sameuls, J. C. and Gale, B. M.; "Effect of Humidity on Performance of Turbojet Engines; NACA Technical Note 2119, June, 1950.
6. Boswell, C. C. and Thurston, S.; "Results of Component Test Program; Hot Cycle Rotor System"; Hughes Tool Company - Aircraft Division Report 285-9-4; August 30, 1957.
7. Keenan, J. H. and Kaye, J.; "Gas Tables"; John Wiley and Sons, Inc.; 1948.
8. Lancaster, O. E.; "Jet Propulsion Engines"; Princeton University Press, 1959.
9. Amer, K. B.; "Whirl Tests, Item 7a"; HTC-AD Report 285-16 (62-16); March 1962.

9. NOMENCLATURE

9.1 Symbols

A	Area
C_d	Discharge coefficient; ratio of actual to ideal discharge; term generally associated with incompressible flow; equals the flow coefficient
C_f	Thrust coefficient; ratio of actual to ideal thrust
C_{vf}	Effective velocity coefficient; ratio of effective velocity assuming complete isentropic expansion to ideal fully expanded velocity
C_w	Flow coefficient; ratio of actual to ideal flow
c_p	Specific heat at constant pressure
EPR	Engine pressure ratio
F	Thrust
g	Acceleration due to gravity
h	Static enthalpy
J	Mechanical equivalent of heat
L	Rotor length; distance from ℄ to nominal center of nozzle: 320 in.
M	Mach number
N_1	Low pressure compressor % speed
N_2	High pressure compressor % speed
NPR	Nozzle pressure ratio based on mass weighted nozzle inlet total pressure
P	Pressure; no subscript for static values
Q_f	Lower heating value of JP-4 fuel; 18,400 Btu/lb
q	Dynamic head (incompressible)
R	Gas constant
r	Radius or radial station

T	Temperature; no subscript for static values
V_T	Rotor Tip Velocity based on 320 in. radius
v	Velocity
w	Flow rate
#	Pounds
	Ratio of specific heats
Δ	Differentail
δ	Pressure parameter; equals P/14.7
η	Efficiency
θ	Temperature parameter; equals T/519
ρ	Density

9.2 Superscripts

—	Mass weighted values
*	Sonic conditions

9.3 Subscripts

a	Air
act	Actual or physical value
amb	Ambient
avg	Average
B	Burner
cf	Pertains to centrifugal force
d,e,f	Station designations for Section 11
edge	Total pressure probe location near wall to pick up "near" boundary layer effects
eff	Effective
oil	Engine lubricating oil
f	Fuel
fs	Flow measuring station in parallel stacks
g	Gross or gas
hub	Hub station below rotating seal

$(\ )_{is}$	Isentropic
LE	Blade leading edge duct
max	Maximum; values along duct centerline
n	Summation digit
nozz	Nozzle inlet plane
sm	Statically measured value (blade tethered)
TE	Blade trailing edge duct
t	Total or stagnation
tot	Total or sum
w	Wall
0	Free stream
1,2	General radial station designations in Section 5
2	Compressor inlet station
7	Turbine discharge station
I	Branch I from Figure 1
II	Branch II from Figure 1

10. APPENDIX I; FLOW DATA ANALYSIS

This section established the procedures for flow data analysis used in this report. Resulting engine and flow parameters for the tether test are given in Table 3. Note: The dimensions included in this table are those directly read from the instruments or are in engineering absolute quantities to aid quick calculations of other values not directly presented herein.

The use of Nikuradse's data (Reference 1) to determine flow rate affords a simplification and reduces the data analysis effort (See Section 10.2). However, while the velocity profiles are suitably developed at the nozzle inlet station (lead-in duct is straight and has a large length to diameter ratio), a check was made to determine the adequacy of this method at the flow measuring station.

From Figure 20, it is seen that the velocity profiles in Branch II are not quite symmetric and considerably flatter than those due to Nikuradse (See Figure 22). This is attributed to the assymetry of the flow ducts, a relatively short straight lead in, and flow unbalance in the branches (See Section 2). Column 22 of Table 3 indicates that the use of Nikuradse's data leads to a +6 to 7% error. It is concluded, however, that a further check is warranted when the blades are untethered and design flow rates are being measured.

10.1 Flow Measurement

The procedure for determining flow at the twin stack measuring stations (Figure 21) and the nozzle inlets is to assume a turbulent velocity profile similar to those of Nikuradse's. Thus, based on the total pressure at the center of the duct corresponding to maximum velocity and static pressure measurements at the wall, the average velocity can be ascertained once having integrated Nikuradse's profiles to determine the ratio of average to maximum velocity as a function of Reynolds number.

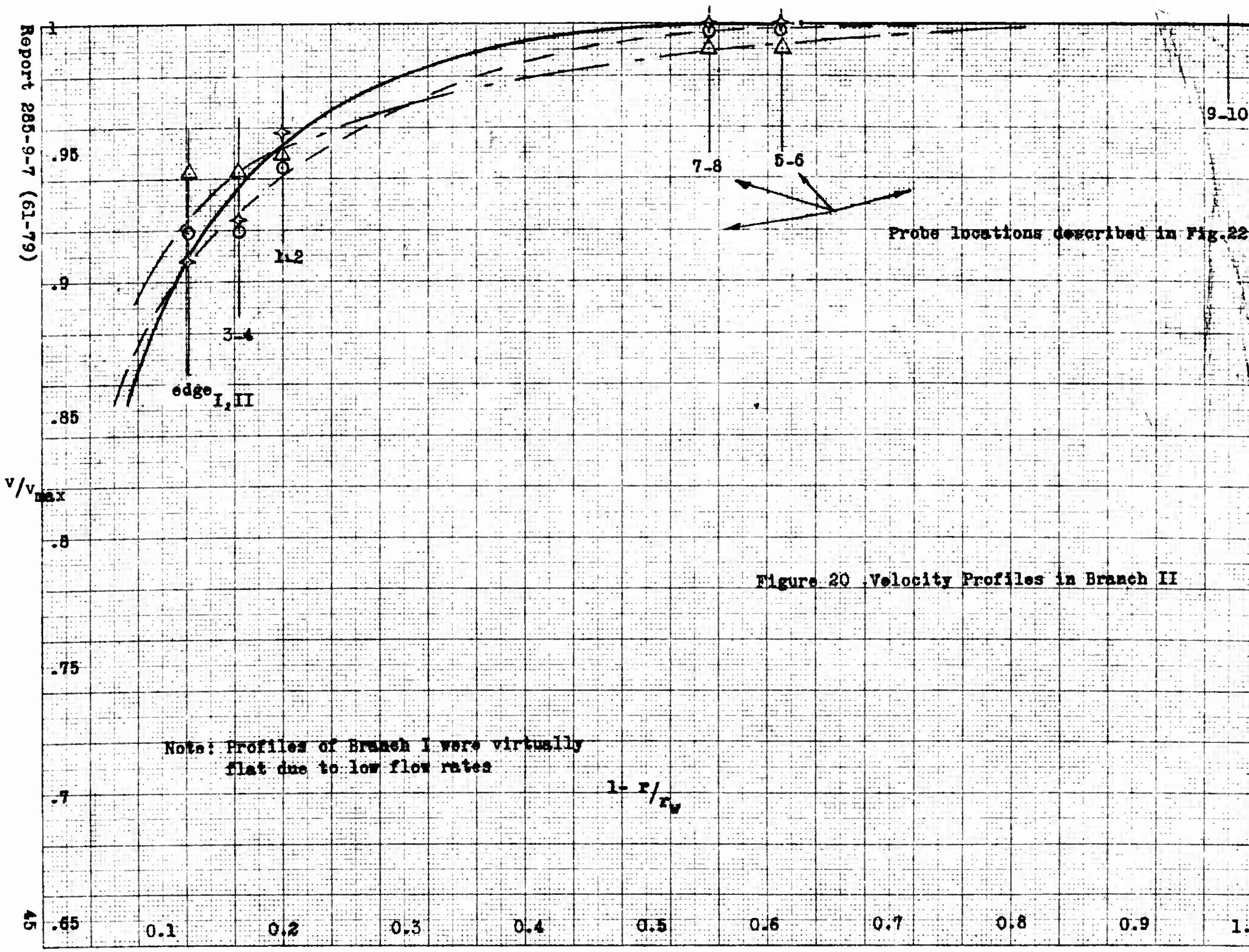

Figure 20 Velocity Profiles in Branch II

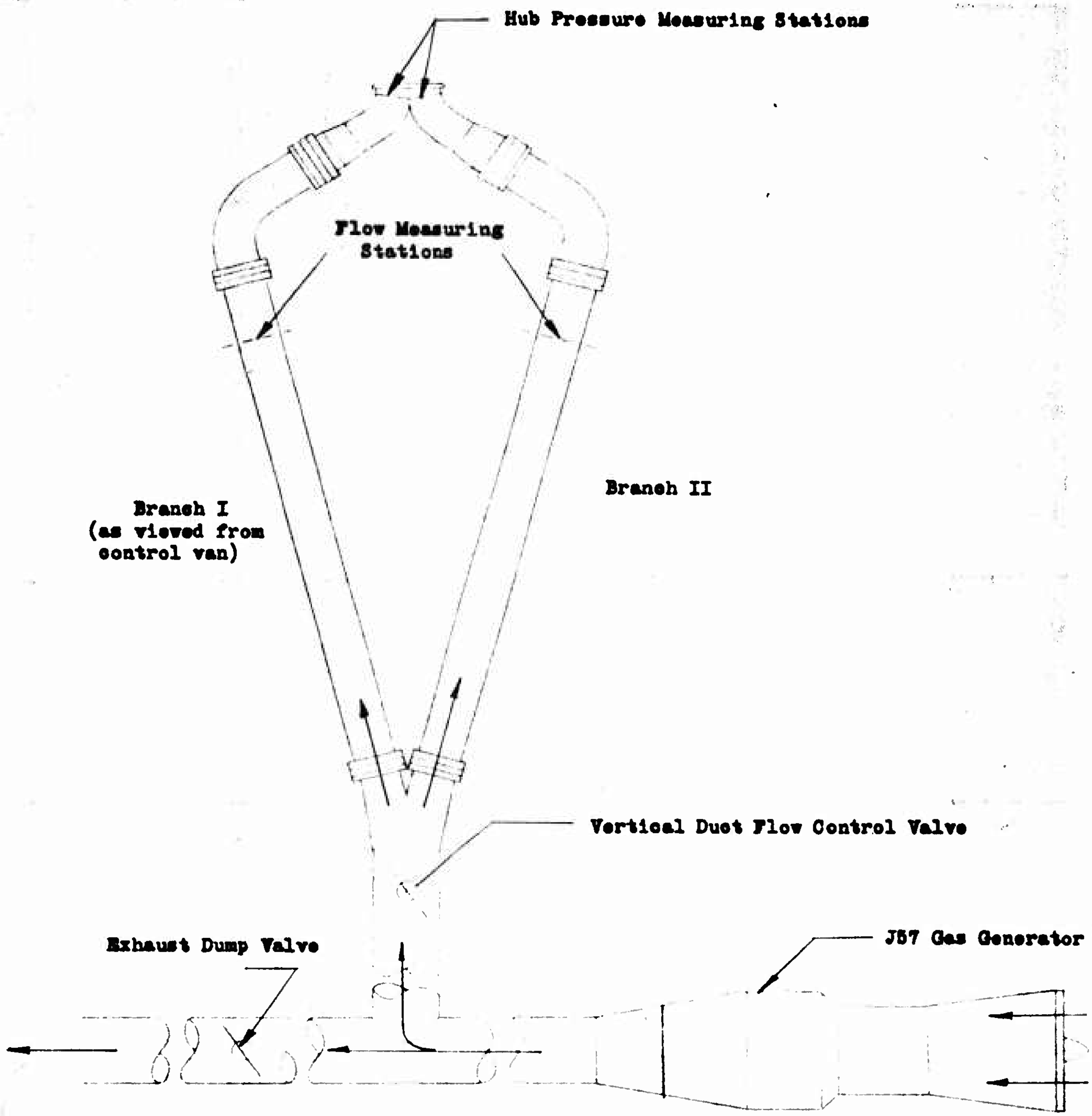

Figure 21. Permanent Streamwise Flow and Pressure Measuring Stations

TABLE 3

J57 ENGINE AND FLOW PARAMETERS
FOR TETHER TEST

Run No.	1	2	3	4	5	6	7	8	9	10	11	12	13
	P_{amb}	T_{amb}	Rel. Hum.	N_1	N_2	w_f	P_{t_7}	T_{t_7}	P_{oil}	T_{oil}	EPR	P_{thub_I}	$P_{thub_{II}}$
	psfa	°F	%	%	%	#/sec	psfa	°R	psig	°C		psfa	psfa
1	2117	72	71	70.0	84.2	0.750	3197	1148	47	49	1.510	3020	2972
2	2118	72	71	71.0	86.0	0.833	3457	1242	47	50	1.632	3291	3230
3	2118	74	65	75.0	88.5	1.111	3774	1310	47	50	1.782	3573	3505
4	2118	74	65	88.0	90.2	1.278	3990	1370	47	50	1.884	3806	3729
5	2118	75	62	80.0	91.5	1.333	4206	1410	47	50	1.986	3986	3908
6	2118	75	62	81.2	93.5	1.528	4552	1495	48	50	2.149	4309	4227
7	2118	75	62	100	96.9	1.944	4854	1485	48	50	2.292	4587	4499
8	2118	75	62	84.0	96.0	1.750	4955	1520	48	53	2.339	4735	4623
9	2118	75	62	83.2	95.8	1.722	4984	1580	48	54	2.353	4727	4630
10	2111	76	62	99.2	96.0	1.889	4636	1455	48	49	2.196		
11	2111	76	62	95.2	94.5	1.667	4240	1390	48	50	2.009		
12	2109	73	73	92.5	96.5	1.944	4950	1550	48	47	2.347		
13	2109	73	73	92.0	96.8	1.931	4980	1560	48	49	2.361	4737	4633
14	2109	73	73	92.0	96.8	1.931	4980	1550	48	49	2.361	4727	4624
15	2108	73	73	88.4	94.8	1.667	4534	1485	48	50	2.151		
16	2108	73	73	87.8	94.3	1.667	4534	1485	48	50	2.151		
17	2108	73	73	87.8	94.3	1.653	4534	1495	48	50	2.151		
18	2108	73	73	90.8	93.8	1.611	4329	1415	48	50	2.054		
19	2108	73	73	91.0	94.0	1.611	4364	1420	48	50	2.070		
20	2108	73	73	91.0	94.0	1.611	4378	1425	48	50	2.077		
21	2108	73	73	87.0	91.8	1.389	3996	1340	47	50	1.896		
22	2107	73	73	87.2	91.8	1.389	3996	1340	47	50	1.897		
23	2107	69	85	90.2	96.2	1.931	4929	1560	48	43	2.339	4689	4585
24	2107	69	85	89.9	96.3	1.931	4957	1560	48	45	2.353	4724	4618
25	2107	69	85	89.9	96.3	1.931	4950	1560	48	45	2.349	4715	4613
26	2107	69	85	90.0	96.3	1.917	4985	1560	48	45	2.366	4748	4649
27	2107	69	85	77.5	89.2	1.194	3719	1360	47	50	1.765	3526	3449

TABLE 3 (Contd.)

J57 ENGINE AND FLOW PARAMETERS FOR TETHER TEST

Run No.	14	15	Nikuradse Method 16	17	18	Area Integration 19	20	21	22	Leading Edge 23	24	25	26
	$T_{tI_{fs}}$	$T_{tII_{fs}}$	w_I	w_{II}	w_{tot}	w_I	w_{II}	w_{tot}	Error $\frac{21-18}{21}$x100	$P_{t_{max}}$	P_t	T_t	$\overline{NPR}$
	°R	°R	#/sec	#/sec	#/sec	#/sec	#/sec	#/sec	%	psfa	psfa	°R	
1	1025	1064	1.21	6.21	7.42	1.45	6.49	7.94	6.5	2716	2676	1018	1.264
2	1115	1160	1.28	6.96	8.24	1.54	7.24	8.78	6.2	2909	2861	1090	1.351
3	1182	1222	2.59	7.65	10.24	3.07	7.98	11.05	7.3	3109	3076	1180	1.452
4	1226	1275	2.36	8.31	10.67	2.80	8.63	11.43	6.6	3290	3218	1230	1.519
5	1055	1075	3.30	9.54	12.84	3.88	9.90	13.78	6.8	3449	3372	1060	1.592
6	1061	1078	3.07	10.15	13.22	3.61	10.62	14.23	7.1	3725	3646	1060	1.721
7	1030	1074	3.96	10.52	14.48	3.74	11.86	15.60	7.2	3949	3874	1068	1.829
8	1127	1080	3.14	10.81	13.89	3.68	11.25	14.93	7.0	4078	3980	1072	1.879
9	1129	1180	3.13	11.03	14.16	3.69	11.30	14.99	5.5	4086	3989	1150	1.883
10										3745		1130	
11										3306		1125	
12										3813		1150	
13	1188	1228								3827		1190	
14	1228	1278								3834		1235	
15										3459		1215	
16										3487		1180	
17										3523		1150	
18										3509		1135	
19										3537		1180	
20										3536		1225	
21										3229		1135	
22										3225		1170	
23	1220	1273											
24	1185	1220											
25	1145	1175											
26	1060	1078											
27	1173	1220											

TABLE 3 (Contd.)

J57 ENGINE AND FLOW PARAMETERS FOR TETHER TEST

Run No.	27	28 Trailing Edge	29 Trailing Edge	30 Trailing Edge	31	32	33	34	35	36	37	38	39	40
	w	$P_{t_{max}}$	$\bar{P}_t$	T_t	NPR	w	w_{tot} =27+28	Error $\frac{21-33}{21}$x100	W_{a_2}	W_f/W_{a_2}	% Theo Dry Air	% H_2O	γ	R
	#/sec	psfa	psfa	°R		#/sec	#/sec	%	#/sec		%	%		#ft/#°R
1	4.06	2783	2736	1018	1.292	4.42	8.48	- 6.8	84.06	0.0089	760	0	1.373	53.35
2	4.46	2997	2940	1095	1.388	4.83	9.29	- 5.3	80.46	0.0104	655	0	1.367	53.35
3	3.93	3208	3144	1180	1.484	5.07	9.00	+18.6	97.74	0.0114	596	0	1.361	53.35
4	5.38	3403	3224	1230	1.569	5.13	10.51	+ 8.0	103.94	0.0123	551	0	1.356	53.35
5	6.15	3563	3481	1070	1.644	6.32	12.47	- 9.5	103.30	0.0129	525	8.9	1.357	56.12
6	6.52	3831	3740	1065	1.766	6.93	13.45	+ 5.5	107.22	0.0143	476	8.7	1.357	55.97
7	6.55	4069	3971	1068	1.875	7.36	13.91	+10.8	138.00	0.0141	481	8.7	1.357	55.97
8	7.49	4198	4093	1068	1.932	7.78	15.27	- 2.3	119.45	0.0147	463	9.0	1.357	56.05
9	7.20	4206	4103	1150	1.937	7.43	14.63	+ 2.4	110.33	0.0156	434	8.0	1.351	55.78
10		3872		1128										
11		3441		1125										
12		3955		1150										
13		4004		1193										
14		4011		1240										
15		3622		1215										
16		3639		1180										
17		3678		1150										
18		3636		1140										
19		3657		1180										
20		3685		1225										
21		3352		1135										
22		3352		1170										

TABLE 3 (Contd.)

J57 ENGINE AND FLOW PARAMETERS FOR TETHER TEST

Run No.	41	42	43	Leading Edge 44	45	46	Trailing Edge 47	48	49	50	51	52
	C_{vf}	C_f	C_w	P_t	$\overline{NPR}$	w	$\bar{P}_t$	$\overline{NPR}$	w	C_{vf}	C_f	C_w
1	0.831	0.482	0.580									
2	0.934	0.607	0.650									
3	0.991	0.657	0.663									
4	0.972	0.756	0.778									
5	0.916	0.772	0.843									
6	0.941	0.853	0.906	3632	1.715	6.38	3722	1.757	6.76	0.968	0.837	0.865
7	0.966	0.876	0.907	3863	1.824	6.41	3950	1.865	7.19	0.974	0.868	0.891
8	0.929	0.897	0.966	3960	1.875	7.30	4067	1.920	7.59	0.950	0.897	0.944
9	0.959	0.918	0.957	3971	1.875	7.04	4085	1.929	7.28	0.974	0.910	0.934

First Iteration ←→ Second Iteration

TABLE 3 (Contd.)

J57 ENGINE AND FLOW PARAMETERS FOR TETHER TEST

Blockage Corrected Values

Run No.	53 C_{vf}	54 C_f	55 C_w
1			
2			
3			
4			
5			
6	0.982	0.877	0.892
7	0.989	0.908	0.918
8	0.964	0.937	0.971
9	0.989	0.950	0.961

Due to the short straight section leading into the stack measuring stations, additional total probes are provided to calibrate the profiles against those of Nikuradse. Also, an evaluation of flow at the nozzle inlet station must be based on hydraulic diameter since the blade ducts are non-circular and are thus different from Nikuradse's.

Nikuradse's velocity profiles for several values of Reynolds number are given in Figure 22. Included also on this figure are the radii at which pressure and temperature measurements are made at the stack measuring stations. Figure 23 presents the ratio of average to maximum velocity as a function of Reynolds number (Reference 1).

The analysis initially assumes the values of gas constant R and ratio of specific heats γ to be 53.35 ft-lb/lb^{o}R and 1.35 respectively. All analysis dependent values reported herein except those identified in Table 3 and the nozzle coefficient figures are 1st iteration values as it is felt that they are representative and additional iteration is not merited. The nozzle coefficients show about a 2 to 4% effect between iterations and therefore both values are provided for reference. The actual values are dependent on fuel-air combustion ratio, temperature, and water content. The corrected R and γ values are presented in Figures 24 and 25 and necessitate iterative analyses when they differ appreciably from the assumed values.

To determine the percentage of water in the primary stream caused by ambient humidity and cooling water injection, an enthalpy balance across the engine is made. This enthalpy balance establishes the engine air ingestion rate while ambient conditions and Figure 26 provide the water percentage due to humidity. The cooling water injection rates are measured directly to complete the input requirements (Figure 27).

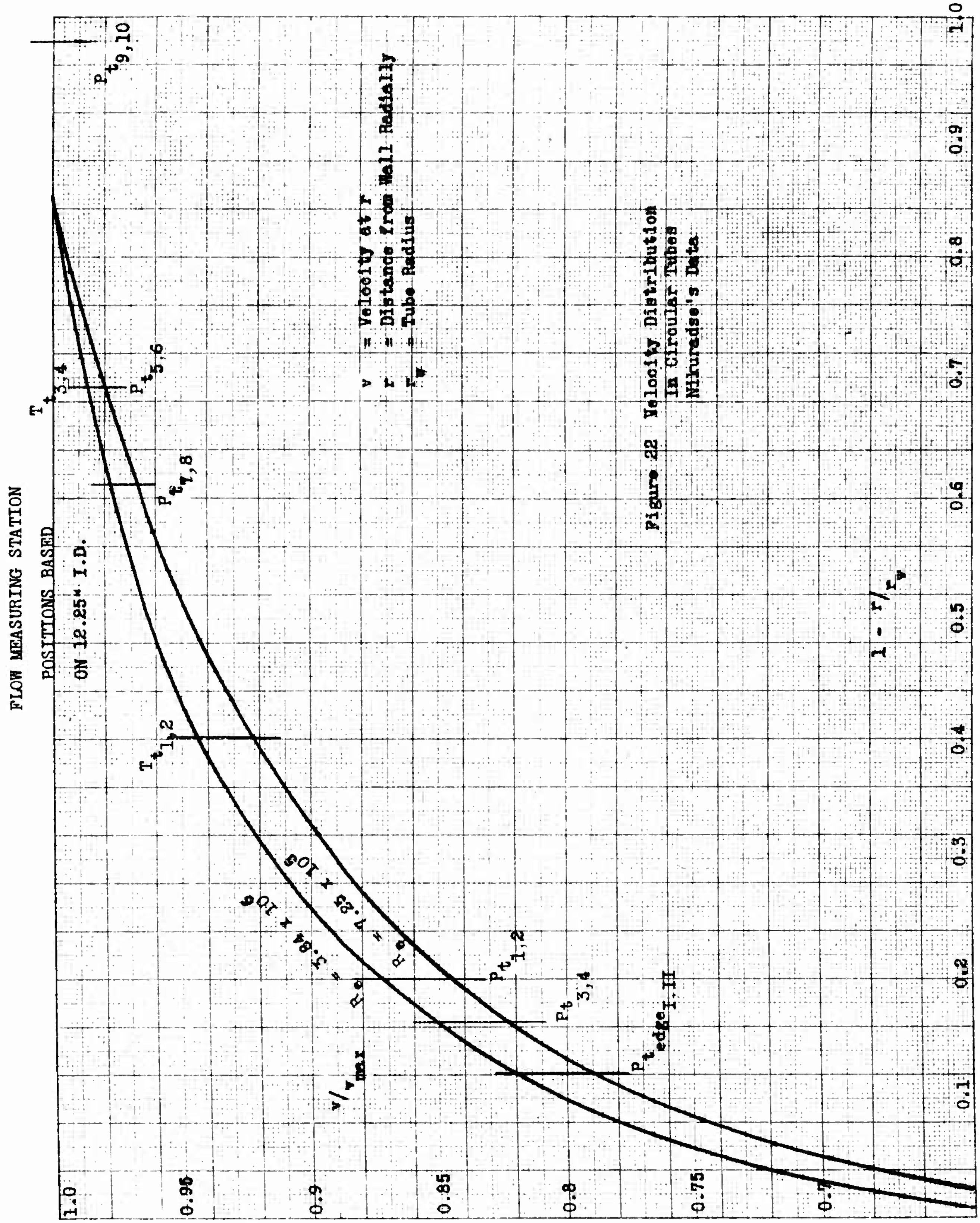

Figure 22 Velocity Distribution In Circular Tubes Nikuradse's Data

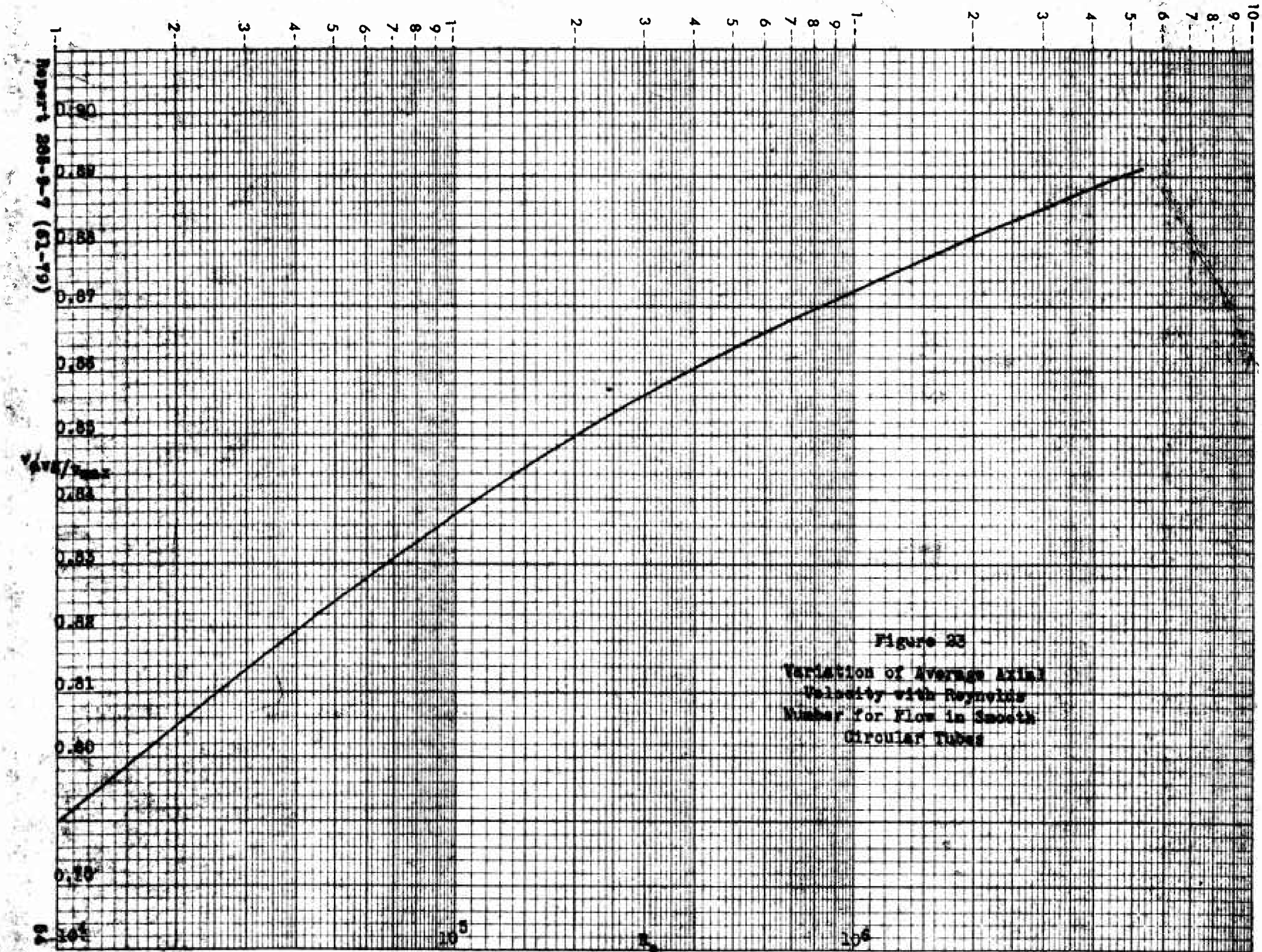

Figure 33

Variation of Average Axial Velocity with Reynolds Number for Flow in Smooth Circular Tubes

Report 285-9-7 (61-79)

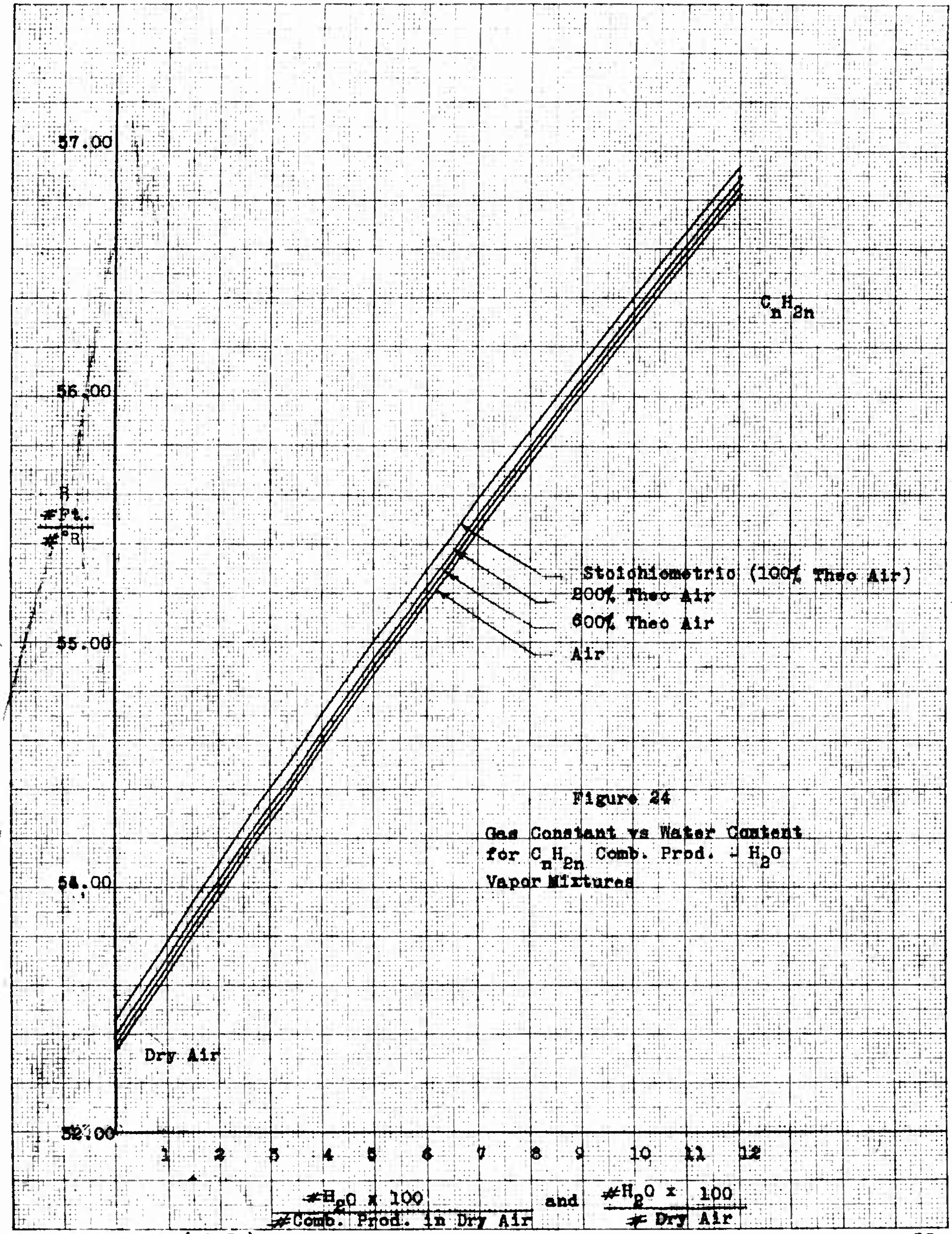

Figure 24

Gas Constant vs Water Content for C_nH_{2n} Comb. Prod. + H_2O Vapor Mixtures

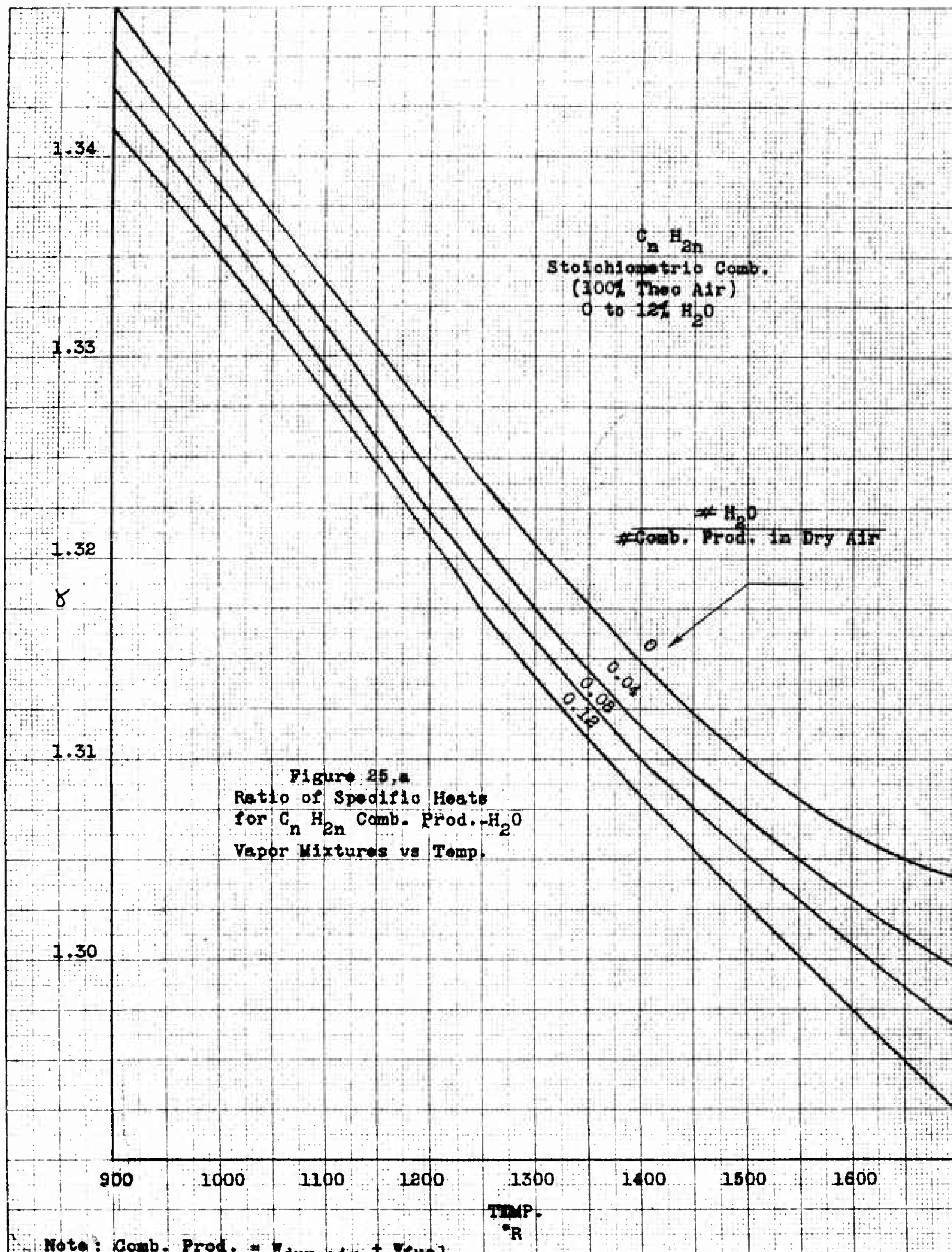

Figure 25,a
Ratio of Specific Heats
for $C_n H_{2n}$ Comb. Prod.-H_2O
Vapor Mixtures vs Temp.

Note : Comb. Prod. = $w_{dry\ air} + w_{fuel}$

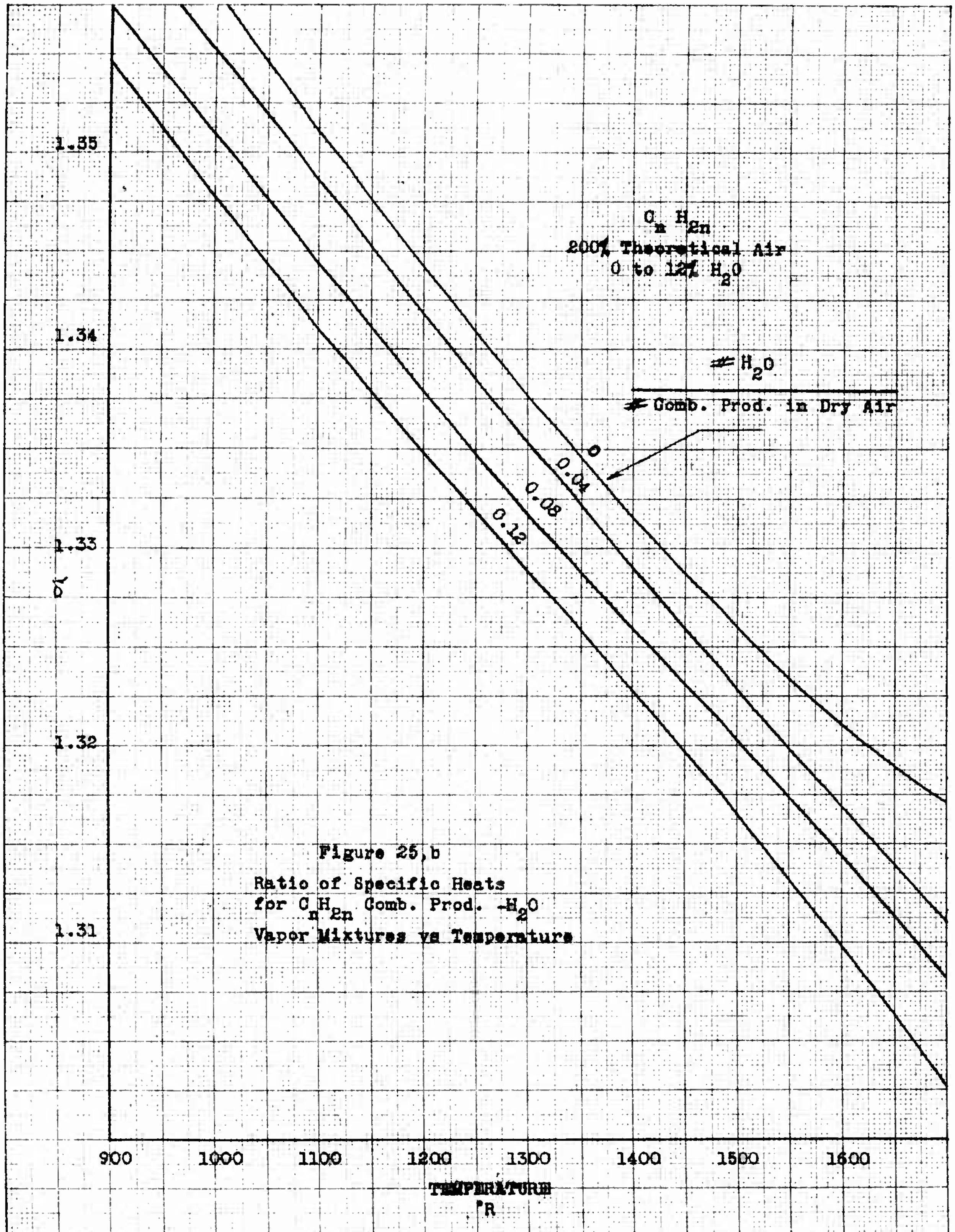

1.35
1.34
1.33
1.32
1.31
γ
C_nH_{2n}
200% Theoretical Air
0 to 12% H_2O
H_2O
Comb. Prod. in Dry Air
0
0.04
0.08
0.12
Figure 25,b
Ratio of Specific Heats
for C_nH_{2n} Comb. Prod. -H_2O
Vapor Mixtures vs Temperature
900
1000
1100
1200
1300
1400
1500
1600
TEMPERATURE
°R

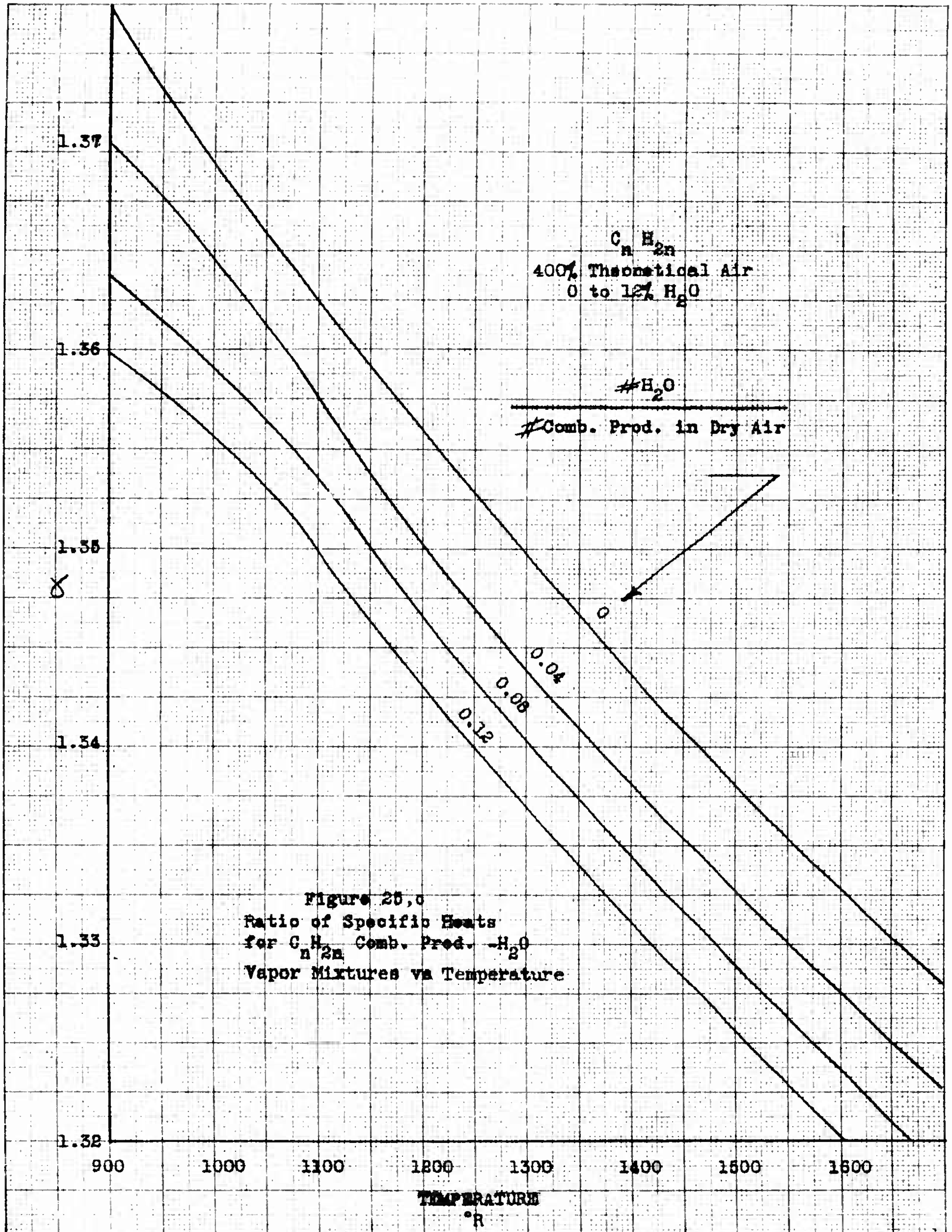

Figure 25,c
Ratio of Specific Heats
for C_nH_{2n} Comb. Prod. $-H_2O$
Vapor Mixtures vs Temperature

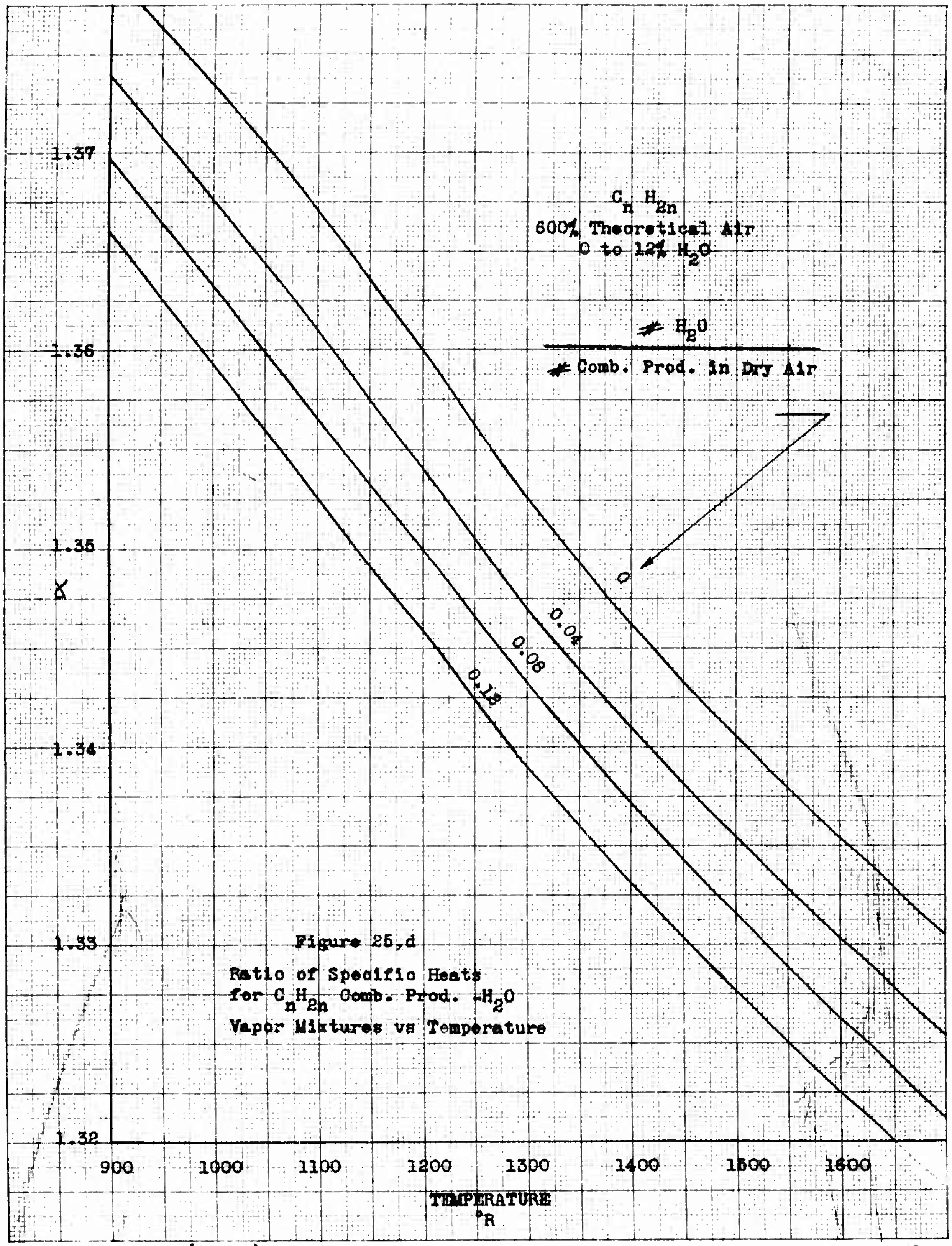
1.37
1.36
1.35
1.34
1.33
1.32
κ
$C_n H_{2n}$
600% Theoretical Air
0 to 12% H_2O
H_2O
Comb. Prod. in Dry Air
0
0.04
0.08
0.12
Figure 25,d
Ratio of Specific Heats for C_nH_{2n} Comb. Prod. -H_2O Vapor Mixtures vs Temperature
900
1000
1100
1200
1300
1400
1500
1600
TEMPERATURE
°R

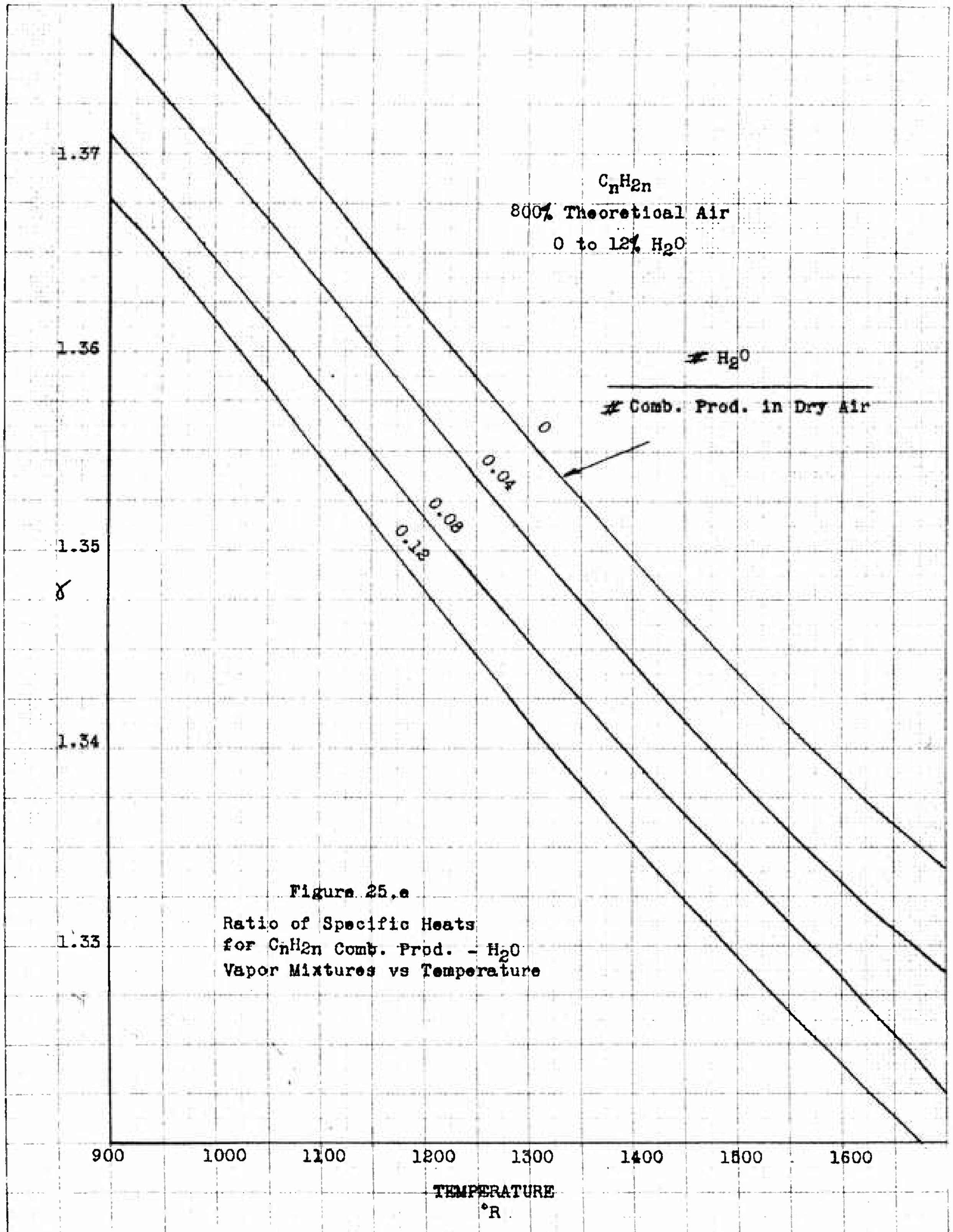

Figure 25.e

Ratio of Specific Heats for C_nH_{2n} Comb. Prod. - H_2O Vapor Mixtures vs Temperature

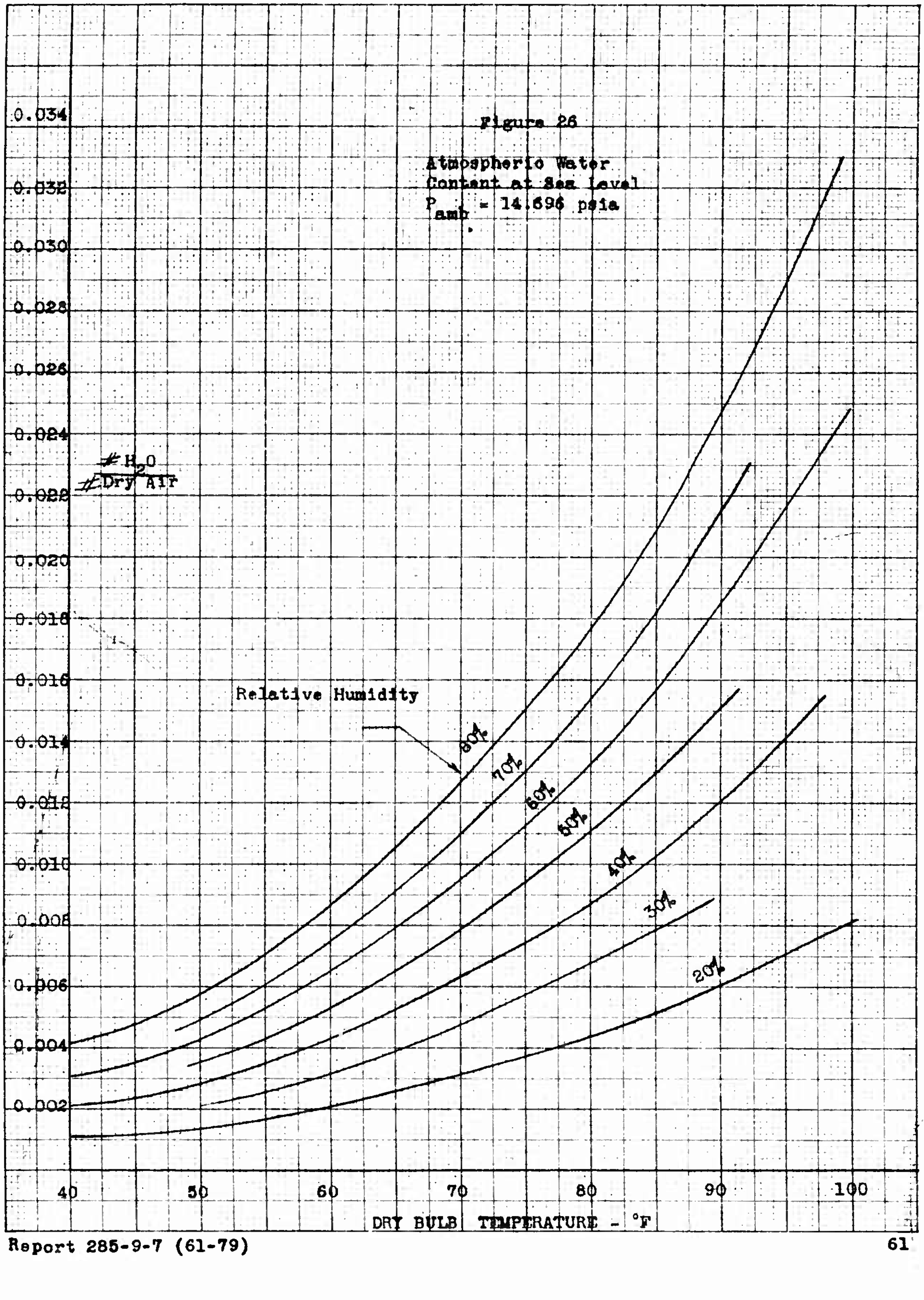
Figure 26
Atmospheric Water
Content at Sea Level
P_{amb} = 14.696 psia
$\frac{\# H_2O}{\# Dry\ Air}$
0.034
0.032
0.030
0.028
0.026
0.024
0.022
0.020
0.018
0.016
0.014
0.012
0.010
0.008
0.006
0.004
0.002
Relative Humidity
80%
70%
60%
50%
40%
30%
20%
40
50
60
70
80
90
100
DRY BULB TEMPERATURE - °F

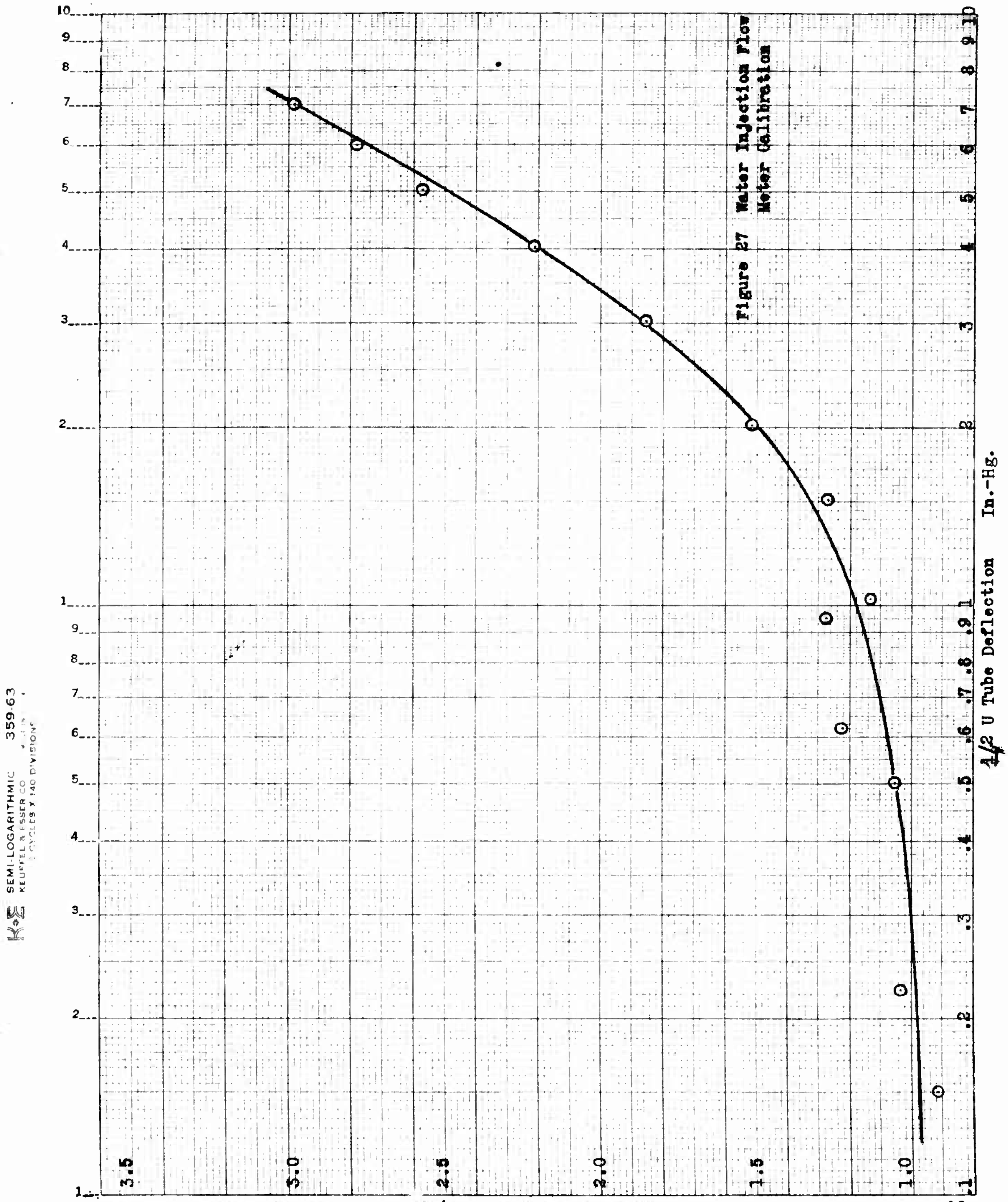

Figure 27 Water Injection Flow Meter Calibration

Ignoring compressor and turbine mechanical losses, a cycle enthalpy balance across the engine may be written as follows:

$$w_{a_2} h_2 + \eta_B Q_f w_f = h_7 w_7 . \tag{1}$$

The engine air ingestion rate is then

$$w_{a_2} = \frac{(\eta_B Q_f - h_7) w_f}{h_7 - h_2} . \tag{2}$$

The results for each run are presented in Table 3 for which the assumed values for calculation are

Q_f = 18,400 Btu/lb

η_B = 0.96

h_2 = dry air values (Ref. 7)

h_7 = 400% theoretical air ($C_n H_{2n}$) values (Ref. 7)

10.2 Mass Weighted Nozzle Inlet Total Pressure

In order to establish a number of nozzle coefficients, a knowledge of nozzle inlet total pressure is required. For many cases, the velocity profile entering the nozzle is sufficiently flat to cause negligible error when using an average inlet total pressure based on several measurements in the nozzle inlet plane. For the rotor tip nozzles which are fed by ducts having a large length to diameter ratio, however, the nozzle inlet velocity profile provides quite a variation in cross section total pressure and necessitates an integration to determine the nozzle inlet mass weighted total pressure.

For $M \leq 0.5$, the difference between total and static pressure may be approximated by

$$P_t - P \approx (1 + \frac{M^2}{4})q \tag{3}$$

or

$$P_t - P \approx \left[1 + \frac{1}{2(\gamma-1)} (\frac{T_t}{T} - 1)\right] q \; .$$

Reducing the flow ducts to their circular cylindrical equivalents, the mass weighted total pressure is defined by

$$\overline{P}_t = \frac{\int_o^{r_w} P_t \, dw}{\int_o^{r_w} dw} = P + \frac{\int_o^{r_w} \left[1 + \frac{1}{2(\gamma-1)} (\frac{T_t}{T} - 1)\right] \frac{\rho v^2}{2g} \, 2\pi \, r \, dr \, v \, \rho}{\int_o^{r_w} 2\pi \, r \, dr \, v \, \rho} \tag{5}$$

which may be approximated by (γ and R assumed constant across the duct),

$$\overline{P}_t \approx P \left\{1 + \frac{\frac{1}{2RT_{max}} \left[1 + \frac{1}{2(\gamma-1)} (\frac{T_t}{T_{max}} - 1)\right] \int_o^{r_w} v^3 \, r \, dr}{\int_o^{r_w} v \, r \, dr}\right\} \tag{6}$$

where T_{max} is based on M_{max} at the center of the duct. For the present study, this leads to an estimated $\overline{P}_t$ which is less than 0.2% greater than the value received from an exact integration of Equation (5).

The universal velocity distribution for turbulent flow in smooth circular tubes is given by Reference 1 as

$$\frac{v}{v_{max}} = 1 - 0.204 \, (\frac{r}{r_w})^2 - 0.250 \, (\frac{r}{r_w})^{32} \tag{7}$$

Substitution of Equation (7) into (6) and integrating leads to

$$\overline{P}_t = P \left\{1 + 0.402 \left[1 + \frac{1}{2(\gamma-1)} (\frac{T_t}{T_{max}} - 1)\right] \frac{v^2_{max}}{g \, R \, T_{max}}\right\} \tag{8}$$

and for $\gamma = 1.35$, $R = 53.35\#\ ft/\#°R$, and $\rho_{max} = \frac{P}{R \, T_{max}}$

$$\overline{P}_t = P + 0.803 \left[1 + 1.428 \, (\frac{T_t}{T_{max}} - 1)\right] q_{max} . \tag{9}$$

11. APPENDIX II; DERIVATION OF NOZZLE COEFFICIENTS

11.1 Effective Velocity Coefficient

The effective velocity coefficient is defined as the ratio of the effective velocity assuming complete expansion to the isentropic fully expanded velocity or,

$$C_{vf} = \frac{\dfrac{F_g}{w_{g/g}}}{(v_f)_{is}} = \frac{v_{eff}}{(v_f)_{is}} = \frac{\int^{Ae} \left[\rho v_e^2 + (P_e - P_f)\right] dA}{(v_f)_{is} \; (w_{g/g})}, \qquad (1)$$

where the symbols are defined in Section 9 and the flow stations are given by Figure 28. Use of this equation is as follows:

a. F_g, W_g, T_{t_d} is measured as a function of nozzle pressure ratio

b. The isentropic fully expanded velocity is defined as

$$(v_f)^2_{is} = \frac{2g \; T_{t_d} \gamma R}{\gamma - 1} \left[1 - \left(\frac{P_f}{P_{t_d}}\right)^{\frac{\gamma - 1}{\gamma}}\right]. \qquad (2)$$

c. Substitution in Equation (1) results as

$$C_{vf} = \frac{F_g}{w_g \sqrt{\dfrac{2 \, T_{t_d} \gamma \, R}{g \, (\gamma - 1)} \left[1 - \left(\dfrac{P_f}{P_{t_d}}\right)^{\frac{\gamma - 1}{\gamma}}\right]}} \qquad (3)$$

Note: $\dfrac{P_f}{P_{t_d}} = \dfrac{1}{NPR}$

d. For $\gamma = 1.35$ and $R = 53.35$ #ft/#°R

$$C_{vf} = \frac{0.280 \; F_g}{w_g \sqrt{T_{t_d} \left[1 - \left(\dfrac{P_f}{P_{t_d}}\right)^{0.259}\right]}} \qquad (4)$$

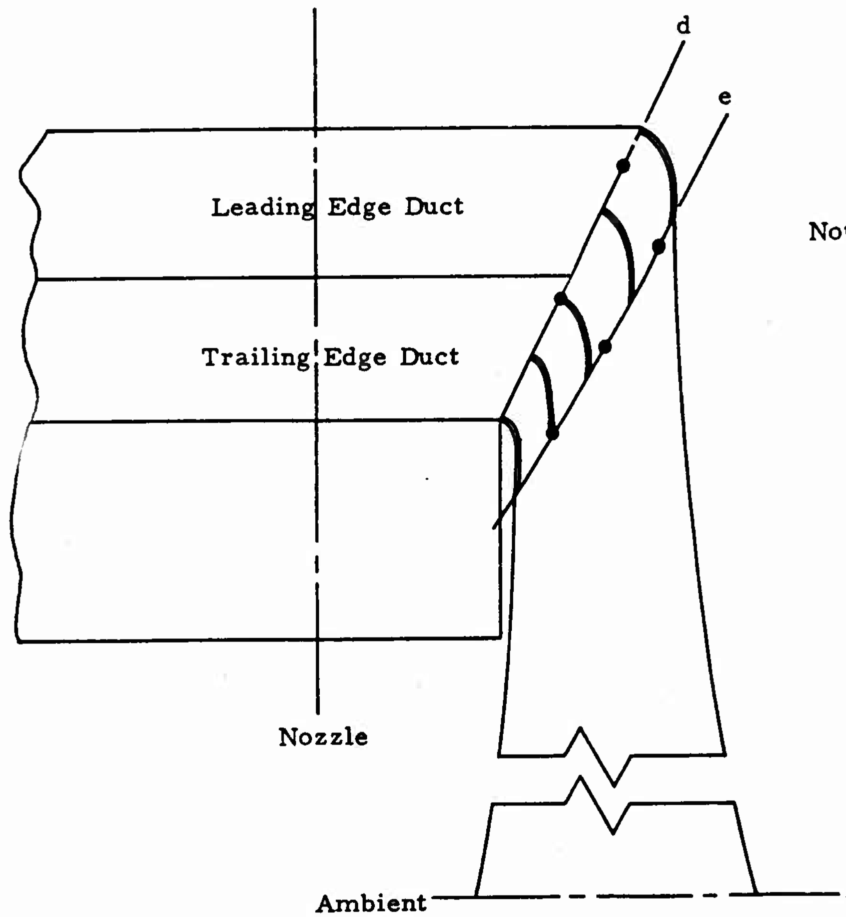

Note: a) Stations d, e, f are the normal reference planes while the other Stations are test equivalents.

Figure 28. Station Designations for Nozzle Coefficient Derivations

e. For unchoked conditions, an alternate form of the isentropic fully expanded velocity is convenient. Since $(P_f)_{is} = (P_e)_{is}$ for unchoked conditions

$$(v_e)^2_{is} = \gamma g R T_{t_d} (M_e)^2_{is} ,$$

where,

$$(M_e)^2_{is} = \frac{2}{\gamma - 1} \left[\left(\frac{P_{t_d}}{P_f} \right)^{\frac{\gamma - 1}{\gamma}} - 1 \right] .$$

Substituting in Equation (1)

$$C_{vf} = \frac{F_g}{w_g M_e} \sqrt{\frac{g}{\gamma R T_e}} . \qquad (5)$$

Finally, for $\gamma = 1.35$ and $R = 53.35$ #ft/#°R

$$C_{vf} = \frac{0.668 \ F_g}{w_g M_e \sqrt{T_e}} . \qquad (6)$$

11.2 Thrust Coefficient

The nozzle thrust coefficient is defined as the ratio of actual to ideal thrust or,

$$C_f = \frac{F_g}{(F_g)_{is}} = \frac{\int^{A_e} \frac{v_e \ dw_g}{g} + (P_e - P_f) \ d \ A}{\left(\frac{w_g \ v_f}{g} \right)_{is}} \qquad (7)$$

To establish the variables for Equation (7)

a. Measure the theoretical exit area A_e and measure F_g as a function of nozzle pressure ratio.

b. For choked conditions, the ideal flow rate based on the measured exit area is

$$(w_g)_{is} = (w_g)^*_{is} = P_{t_d} A_e \sqrt{\frac{\gamma g}{T_{t_d} R}} \left(1 + \frac{\gamma - 1}{2}\right)^{-\frac{\gamma + 1}{2(\gamma - 1)}} . \qquad (8)$$

The isentropic velocity for full expansion is

$$(v_f)_{is} = \left\{2gJc_p T_{t_d}\left[1 - \left(\frac{P_f}{P_{t_d}}\right)^{\frac{\gamma - 1}{\gamma}}\right]\right\}^{1/2} = \left\{\frac{2gT_{td} R\gamma}{\gamma - 1}\left[1 - \left(\frac{P_f}{P_{t_d}}\right)^{\frac{\gamma - 1}{\gamma}}\right]\right\}^{1/2} . \qquad (9)$$

Employing Equations (8) and (9), the isentropic thrust is then

$$(F_g)_{is} = \left(\frac{w_g v_f}{g}\right)_{is} = P_{t_d} A_e \gamma \left(1 + \frac{\gamma - 1}{2}\right)^{-\frac{\gamma + 1}{2(\gamma - 1)}} \left\{\frac{2}{\gamma - 1}\left[1 - \left(\frac{P_f}{P_{t_d}}\right)^{\frac{\gamma - 1}{\gamma}}\right]\right\}^{1/2} . \qquad (10)$$

For $\gamma = 1.35$, the nozzle thrust coefficient becomes

$$C_f = \frac{0.532 \; F_g}{P_{t_d} A_e \left[1 - \left(\frac{P_f}{P_{t_d}}\right)^{0.259}\right]^{0.5}} . \qquad (11)$$

Note: $P_f = P_{amb}$.

c. For unchoked conditions, the ideal flow rate for expansion to ambient conditions is given by

$$(w_g)_{is} = P_{t_d} A_e \sqrt{\frac{\gamma g}{R T_{t_d}}} \left(1 + \frac{\gamma - 1}{2} M_e^2\right)^{-\frac{\gamma + 1}{2(\gamma - 1)}} . \qquad (12)$$

Combining with Equation (9), the ideal thrust is

$$(F_g)_{is} = \left(\frac{w_g v_f}{g}\right)_{is} = P_{t_d} A_e \gamma \left(1 + \frac{\gamma - 1}{2} M_e^2\right)^{-\frac{\gamma + 1}{2(\gamma - 1)}} \left\{\frac{2}{\gamma - 1}\left[1 - \left(\frac{P_f}{P_{t_d}}\right)^{\frac{\gamma - 1}{\gamma}}\right]\right\}^{1/2} . \qquad (13)$$

and, with Equation (7) for $\gamma = 1.35$, the nozzle thrust coefficient becomes

$$C_f = \frac{0.31\, F_g \left(1 + 0.175\, M_e^2\right)_{is}^{3.357}}{P_{t_d}\, A_e \left[1 - \left(\frac{P_f}{P_{t_d}}\right)^{0.259}\right]^{0.5}} \quad . \tag{14}$$

11.3 Flow Coefficient

The nozzle flow coefficient is defined as the actual to ideal flow or,

$$C_w = \frac{w_g}{(w_g)_{is}} = \frac{\int^{A_e} g \rho v \, dA}{(w_g)_{is}} \quad . \tag{15}$$

Also,

$$\frac{C_f}{C_{vf}} = \frac{\dfrac{F_g}{(F_g)_{is}}}{\dfrac{F_g}{\dfrac{w_g/g}{(V_f)_{is}}}} = \frac{\dfrac{w_g}{g}}{\dfrac{F_{g\,is}}{(V_f)_{is}}} = \frac{w_g}{(w_g)_{is}} \quad . \tag{16}$$

Thus,

$$C_w = \frac{C_f}{C_{vf}} \quad . \tag{17}$$